

## Article

# Low-Temperature Fabrication of Flexible Dye-Sensitized Solar Cells: Influence of Electrolyte Solution on Performance under Solar and Indoor Illumination

Roberto Avilés-Betanzos <sup>1</sup>, Gerko Oskam <sup>1,2,\*</sup> and Dena Pourjafari <sup>1,\*</sup>

<sup>1</sup> Departamento de Física Aplicada, Centro de Investigación y de Estudios Avanzados del Instituto Politécnico Nacional, Merida 97310, Yucatan, Mexico; roberto.aviles@cinvestav.mx

<sup>2</sup> Departamento de Sistemas Físicos, Químicos y Naturales, Universidad Pablo de Olavide, 41013 Sevilla, Spain

\* Correspondence: gerko.oskam@cinvestav.mx or gosk@upo.es (G.O.); dpourjafari@cinvestav.mx (D.P.); Tel.: +52-999-942-9429 (G.O.); +52-999-942-9400 (D.P.)

**Abstract:** Flexible photovoltaics is an attractive technology for product-integrated energy supply under both outdoor and interior conditions. In particular, dye-sensitized solar cells (DSSCs) based on flexible plastic conductive substrates provide ample opportunities for unique applications; however, they prevent the use of high-temperature processing steps usually applied in the fabrication of the solar cell. In the first part of this paper, we present an overview of a careful selection of the most relevant work in the field of flexible DSSCs (F-DSSCs), ranging from pioneering methods to the most cutting-edge techniques. Key elements and critical considerations for the design of an efficient F-DSSC are also provided. In the second part, we report the fabrication of DSSCs on both rigid and flexible plastic substrates using low-temperature processing. Three different  $I^-/I_3^-$  electrolyte configurations were tested. Rigid and F-DSSC showed 2.62% and 1.00% efficiency under 1 sun and an output power of 8.60 and 4.00  $\mu\text{W}/\text{cm}^{-2}$  under low-light conditions, respectively. In this work, we report a novel solvent mixture that shows a significant enhancement of the performance of the low-temperature processed configuration, without adding steps in the fabrication process.

**Keywords:** dye-sensitized solar cell; flexible photovoltaics; low-temperature processing



**Citation:** Avilés-Betanzos, R.; Oskam, G.; Pourjafari, D. Low-Temperature Fabrication of Flexible Dye-Sensitized Solar Cells: Influence of Electrolyte Solution on Performance under Solar and Indoor Illumination. *Energies* **2023**, *16*, 5617. <https://doi.org/10.3390/en16155617>

Academic Editor: Peter D. Lund

Received: 29 June 2023

Revised: 19 July 2023

Accepted: 24 July 2023

Published: 26 July 2023



**Copyright:** © 2023 by the authors. Licensee MDPI, Basel, Switzerland. This article is an open access article distributed under the terms and conditions of the Creative Commons Attribution (CC BY) license (<https://creativecommons.org/licenses/by/4.0/>).

## 1. Background and Context

The growth in the world's population, coupled with the ever-increasing energy requirements of modern technological advances, has resulted in an urgent demand for a greater supply of energy [1,2]. On the other hand, the increasing concerns about the environmental consequences associated with traditional energy sources have prompted the scientific community to seek out and develop non-polluting, abundant, and cost-effective energy sources, simultaneously mitigate the effects of climate change, and enable a shift toward a renewable energy-based society in the near future [3,4]. Among all the available sources of renewable energy, solar energy stands out as the one with the greatest potential to meet the demands of our modern world. The sun's energy that reaches the Earth's surface every year amounts to an astounding 3.8 million exajoules, which is more than enough to satisfy the entire global energy demand. Moreover, the use of solar energy for electricity generation is not only environmentally safe, but also exceptionally clean [5]. Hence, photovoltaic (PV) technology has emerged as a promising contender for the future of sustainable electricity production.

Based on the most recent projections, it is anticipated that solar energy could account for 15–30% of the total global electricity production by the year 2050, with PV technology emerging as a vital driving force behind this movement. PV remains at the forefront of this pivotal endeavor, and the developments have led to its categorization into three distinct generations: first, second, and third [6–9].

In this work, our emphasis is on third-generation (3G) solar cells, which have emerged as a major breakthrough in the field of solar cell technology since the 1990s, resulting from over two decades of sustained and intensive research and development [10]. Third generation (3G) is currently generating significant interest in the scientific community due to specific advantages over conventional solar devices, such as potentially lower processing costs, solution-processing manufacturing techniques, shorter payback times, and environmental sustainability. These advantages make them a promising alternative with the potential to produce high-efficiency light-to-electricity conversion devices at a lower cost [11–13]. Third-generation (3G) PV technology is expected to have a significant impact on the renewable energy industry particularly in energy-supporting applications, such as building-integrated PV and other product-integrated and portable devices. It is also well suited for various recent developments, including Internet of Things (IoT) applications [14–16]. This most recent generation of PV systems comprises a diverse collection of state-of-the-art technologies, including organic solar cells (PCE  $\approx$  19.2%), quantum dot solar cells (PCE  $\approx$  18.1%), perovskite solar cells (PCE  $\approx$  26%), and DSSCs (PCE  $\approx$  13%) [17]. However, it is important to note that each of these technologies has its own advantages and disadvantages, which need to be considered.

This work focuses on F-DSSCs, and in the following sections, we provide extensive information on the architecture, functional mechanism, and limitations of this 3G PV technology. Since there are few review papers in the literature addressing the manufacturing challenges and limitations related to flexible solar cells [6,18–23], we provide an overview that summarizes key information on the strategies to overcome these fabrication limitations. Hence, we have divided the paper into two parts. The first part is a mini-review of the most relevant work on F-DSSCs (Sections 2–5). In the second part of this work (Sections 6–9), we present our recent research on the low-temperature fabrication of flexible devices using novel techniques, without any extra steps or post-treatments. The majority of research on these systems focuses on the improvement of the photoelectrode at low temperatures. However, the influence of the electrolyte composition on F-DSSCs performance has not been studied in detail and is not well understood. Here, we demonstrate a novel solvent mixture for an  $I^-/I_3^-$  electrolyte that shows a significant enhancement in the performance of this low-temperature configuration. The optimal electrolyte composition exhibited a favorable effect on the rate of electron injection into the  $TiO_2$  conduction band by the dye. This highlights the potential that the electrolyte holds in improving the performance of low-temperature configurations while avoiding the introduction of additional steps in the fabrication process.

## 2. DSSCs

The DSSC represents the first 3G technology that has attracted substantial attention as an emerging solar technology related to the potential for cost-effectiveness and straightforward manufacturing [16]. These electrochemical devices operate based on principles that resemble photosynthesis in green plants [24]. The initial development of DSSC technology back in 1972 used a chlorophyll-sensitized ZnO solar cell, reaching a low efficiency of only 1% due to incomplete absorption of the incident sunlight with just a single layer of dye molecules [12,25]. A major breakthrough in the field was achieved in 1991, resulting in an efficiency of 7.1% and conversion of approximately 80% of absorbed photons into electrical current thanks to the introduction of a novel dye sensitizer combined with a nanostructured, mesoporous  $TiO_2$  structure developed and reported in Nature by O'Regan and Grätzel [26,27]. Although the seminal work on DSSCs began over 30 years ago, research in this field has recently advanced significantly, with strong efforts being made to improve the efficiency both under outdoor and indoor conditions [28]. This is because of numerous advantages of a DSSC, such as using inexpensive and abundant materials, compatibility with rigid and flexible substrates, and simple, non-vacuum, and high-speed screen-printing fabrication process [4,19,29]. In recent years, there has been a trend toward the fabrication of DSSC on lightweight flexible substrates, such as plastic or metal foils [6,30]. Unlike glass

electrodes, which impose inherent limitations in terms of fragility, weight, and shape [20], F-DSSCs inherit the aesthetic features of rigid DSSCs (translucency and polychromaticity) and can be applied on curved surfaces including clothes, bags, car tops, sensor heads, etc. [13]. More importantly, F-DSSCs offer the potential for significant cost reduction, as they are compatible with large-scale roll-to-roll processing, which is an existing continuous, low-cost industrial method to print DSSCs. In addition, the processes can be performed at low temperature and under atmospheric pressure [4,19,29]. To fulfill the stringent requirements of PV production, high-speed manufacturing processes are crucial to achieve the high volume necessary to meet the demands. In this regard, the utilization of flexible substrates becomes even more significant. By harnessing the benefits of this component, the industry can effectively expedite the production process and achieve the desired high volume required for the successful implementation of PV technologies [31].

Unlike silicon cells, DSSCs are better aligned with the spectral characteristics of indoor lighting, allowing them to effectively harness and convert available light sources for electricity generation in both indoor and outdoor settings [32]. DSSCs exhibit an impressive ability to operate optimally by harnessing available diffuse ambient light, including light during dawn, dusk, and cloudy weather, which often goes unutilized [33]. Remarkably, when subjected to low-intensity irradiation (0.3–0.5 sun), the efficiency of DSSCs is comparable to that of silicon-based solar cells [7,34]. The superior performance under low-intensity illumination and the possibility to optimize the spectral sensitivity to the spectrum emitted by commonly used indoor fluorescent and LED light (400–650 nm) mean that DSSCs are currently considered one of the most suitable options for indoor light-harvesting purposes, resulting in energy conversion efficiencies beyond 32% [8,32,35,36].

### 3. Exploring the Essential Components and Operational Mechanism of DSSC

#### 3.1. DSSC Elemental Structure

The DSSC is composed of four fundamental components that are essential for its effective operation:

1. The photoelectrode consists of a transparent conductive oxide coated substrate onto which a mesoporous oxide layer is deposited. This layer facilitates the transfer of electrons generated by the absorption of sunlight by the sensitizer.
2. The sensitizer is a molecular monolayer of dye that is adsorbed onto the surface of the mesoporous oxide layer. Its function is to harvest incident sunlight and transfer electrons to the oxide.
3. The electrolyte typically consists of an organic solvent that contains a redox mediator. This component is crucial for the regeneration of the dye and the redox electrolyte during operation.
4. The counter electrode is typically a fluorine-doped tin oxide (FTO) or indium tin oxide (ITO) on glass or plastic coated with a catalyst material that facilitates the redox couple regeneration reaction and collects electrons from the external circuit (Figure 1).

In the following section, we provide a detailed analysis of the specific critical functions that are carried out by each of the key components in the operational mechanism of DSSCs.

#### 3.2. DSSC Operational Mechanism

The photoconversion of solar radiation into electrical energy in DSSCs follows a mechanism that resembles the photoinduced electron transfer process that occurs during photosynthesis in plants, which is illustrated in Figure 2. This mechanism is designed to mimic several natural processes, with the dye playing a role similar to that of chlorophyll in plants, which is a unique and distinctive feature of DSSCs. The process of energy conversion is triggered by the absorption of incident photons by the sensitizer, which forms a monolayer adsorbed on the surface of the mesoporous metal oxide. The photon energy is sufficient to generate an electronic excitation within the sensitizer. Ground-state electrons are promoted to an excited state (Process 1), which is often simplified in the literature as the transition from the highest occupied molecular orbital (HOMO) to the lowest unoccupied

molecular orbital (LUMO). Upon excitation, the electrons in the excited state may be at a higher energy and can be transferred to the conduction band of the metal oxide photoanode (Process 2). This results in the formation of a localized “hole” corresponding to the oxidized dye molecule. Note that the term “hole” is generally defined as the mobile positive charge in the valence band of a semiconductor, and as such, “holes” do not play a role in the DSSC. The charge separation at the interface between the dye and metal oxide occurs within a femto to picosecond time frame. The injected electrons diffuse through the nanostructured, mesoporous metal oxide film and reach the transparent conducting oxide film that covers the glass substrate (Process 3). This process occurs within the nanosecond to microsecond timescale. Simultaneously, within the time range of nano to microseconds, the oxidized sensitizer molecules are restored to their ground state via electron donation from a reduced species present in the electrolyte, corresponding to “hole” transfer to the electrolyte (Process 4). Finally, the oxidized redox mediator diffuses to the counter electrode, where the circuit is closed as electrons from the counter electrode that have traversed the external circuit catalyze the reverse reaction of the redox couple (Process 5). Hence, the solar cell is fully regenerative, where the electrons injected and collected move through the external wiring and perform work.

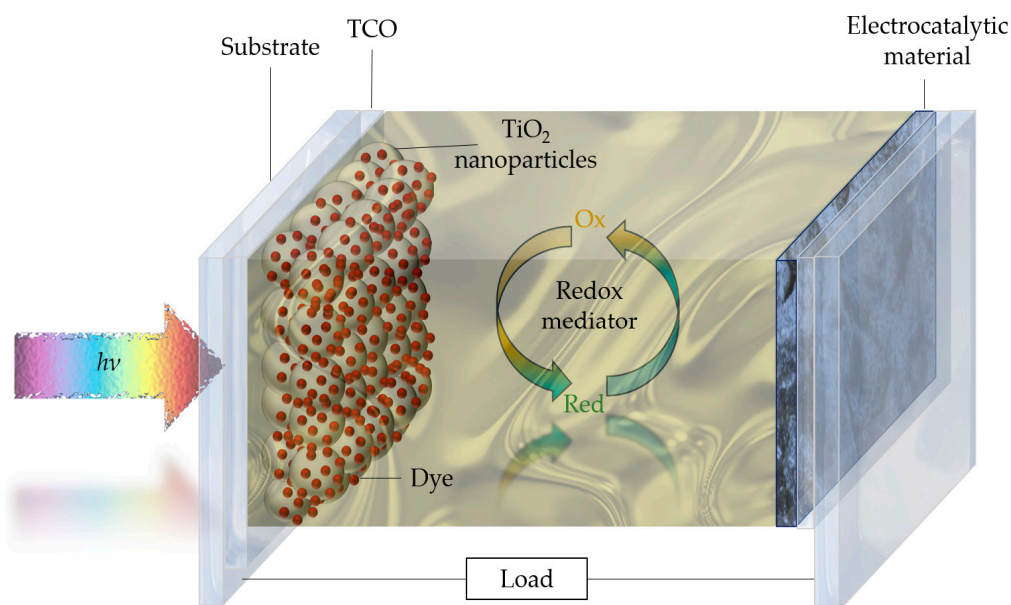


**Figure 1.** Schematic representation of the main components of a DSSC.

### 3.3. Recombination Processes

The prevention of electronic recombination processes is crucial for optimizing the performance of a DSSC. Electronic recombination refers to the undesired recombination of electrons with “holes”, which can significantly impact the efficiency of the device. Several pathways exist for recombination, and addressing these pathways is essential for improving the overall performance of DSSCs. One pathway involves the non-radiative relaxation of electrons in the excited state at the LUMO energy level of the sensitizer, causing them to return to the ground state (Process 6). This phenomenon is often linked to an elevated level of dye molecule aggregation at the metal oxide surface. In this stage, electrons in the LUMO level of the dye can also undergo recombination with the redox electrolyte within a time frame of milliseconds to seconds (Process 7). Furthermore, after injection into the conduction band, electrons need to travel a considerable distance (2–10  $\mu\text{m}$ ) to reach the TCO of the photoanode. During their trajectory, electrons face hurdles that hamper their movement owing to inadequate interparticle connections and/or electronic trap states caused by defects in the metal oxide crystal lattice, generally at the surface. The probability of electron deviation from its desired trajectory increases as it remains in the metal oxide

for an excessive amount of time. This may lead to electrons being either back-transferred to oxidized dye molecules or being transferred to the redox electrolyte surrounding the metal oxide (Processes 8 and 9, respectively). Lastly, electrons that successfully arrive at the anode still need to move across the TCO surface toward the external circuit. If the TCO is in contact with the redox electrolyte, it can undergo loss via the reduction of oxidized species present within the electrolyte (Process 10). In order to prevent these recombination processes, a series of design protocols have been developed for the photoanode, molecular design of dyes, and redox mediators.

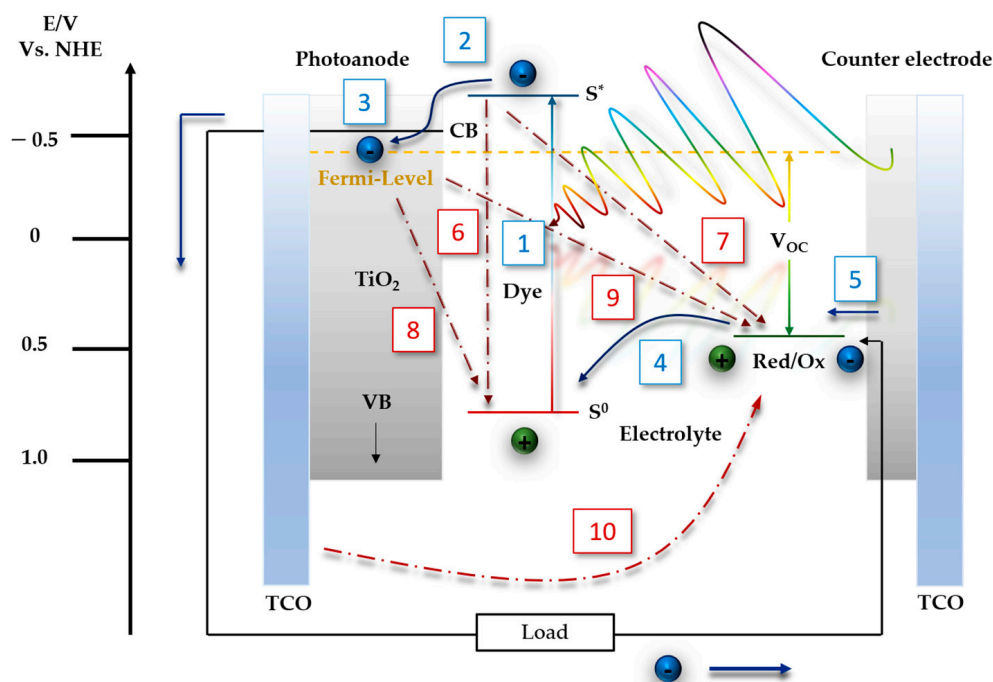


**Figure 2.** Charge flow pathways within a DSSC in an energy diagram. The favorable operating flow is indicated by blue numbers and continuous arrows, while the red numbers and dashed arrows represent various electronic recombination pathways. Blue and green spheres represent electrons and “holes”, respectively.

### 3.4. DSSC PV Parameters

The overall performance of a DSSC under irradiation can be estimated by quantifying its sunlight-to-electric power conversion efficiency ( $\eta$ ). This is commonly measured under standard irradiation conditions ( $100 \text{ mW/cm}^2$ , AM 1.5). The efficiency is defined as the ratio of the maximum generated power ( $P_{\text{max}}$ ) to the maximum incident light power ( $P_{\text{in}}$ ), and can be determined by measuring the current–voltage (J–V) curve as follows:

$$\eta = \frac{P_{\text{max}}}{P_{\text{in}}} \times 100\%, \quad (1)$$

$$\eta(\%) = \frac{V_{\text{OC}} \times J_{\text{SC}} \times \text{FF}}{P_{\text{in}}} \times 100\%, \quad (2)$$

$$\text{FF} = \frac{V_{\text{max}} \times J_{\text{max}}}{V_{\text{OC}} \times J_{\text{SC}}}, \quad (3)$$

where  $J_{\text{SC}}$  is the short-circuit current ( $\text{mA/cm}^2$ ),  $V_{\text{OC}}$  is the open-circuit voltage (V), and FF is the fill factor. The  $V_{\text{OC}}$  is determined by a potential difference between the Fermi level of electrons in the metal oxide and the redox potential of the electrolyte. The  $V_{\text{OC}}$  is defined as the voltage, where J is zero.  $J_{\text{SC}}$  is a key parameter influenced by several factors, such as the incident light harvest efficiency, charge injection efficiency, and charge collection efficiency.

It is the maximum current density that is generated when the cell is under short-circuit zero-bias conditions. The FF in a solar cell is a key performance parameter that exerts a significant influence on the device's efficiency. It is defined as the ratio of the maximum power output to the product of  $V_{OC}$  and  $J_{SC}$ . The maximum power output occurs at the point on the J–V curve, where the voltage and current density are represented as  $V_{max}$  and  $J_{max}$ , respectively [4,9].

#### 4. Flexible Photoelectrodes: Key Design Considerations for Optimal Performance

Among the fundamental components described in Section 3.1, the photoanode assumes a pivotal role in DSSCs, as it performs indispensable functions that encompass the efficient adsorption of dye molecules and effective electron injection and transport processes. A large surface area is required to permit the anchoring of a large density of dye sensitizers, thereby enhancing the light-harvesting efficiency of the solar cell. Additionally, the photoanode acts as a conduit for the transport of photogenerated electrons, requiring efficient charge separation and minimal recombination losses. Consequently, the design and optimization of the photoanode structure and materials are essential for achieving high-performance DSSCs [25]. The photoanode comprises a complex assembly of integral elements that collectively form a synergistic architecture, including a sensitized-semiconductor oxide deposited on a transparent conductive oxide (TCO)-coated substrate [3].

Glass, plastics, and metals are the commonly used substrates in DSSCs. However, in order to meet the criteria for large-scale production, the use of glass substrates is discouraged. Instead, plastic and metal substrates offer viable alternatives across three fundamental configurations of DSSCs [19]. While metal substrates have shown promising efficiencies, they are accompanied by certain limitations, such as susceptibility to corrosion by electrolyte solution components. Hence, careful consideration should be given to the selection of electrolyte components to ensure compatibility with the chosen substrate type. Additionally, the high-temperature sintering process employed with metal substrates can give rise to oxidation concerns, requiring additional steps that complicate large-scale manufacturing processes [37]. The use of metal substrates in DSSCs also has a notable drawback in terms of their lack of transparency. Such DSSCs requires illumination from the front side through the counter electrode, which may lead to a reduction in the conversion efficiency. This can be attributed to the partial reflection/absorption of light, either by the electrocatalyst deposited on the counter electrode or various molecular species within the redox electrolyte solution [25]. Significantly, flexible plastic conductive substrates (FPCSs), such as indium-doped tin oxide polyethylene terephthalate (ITO,  $In_2O_3:Sn$ ) (ITO-PET) and indium-doped tin oxide polyethylene naphthalate (ITO-PEN), offer notable advantages, including flexibility and lightweight properties, rendering them well suited for reel-to-reel (R2R) production techniques. Furthermore, these substrates exhibit satisfactory levels of transparency (80% at 550 nm) and a sheet resistance at approximately  $10 \Omega/\square$ , along with commendable chemical stability within the electrolyte, surpassing the performance of their metal counterparts [18,38].

Extensive research and development efforts have been undertaken to formulate the photoanode in DSSCs, exploring diverse materials such as  $ZnO$ ,  $Nb_2O_5$ ,  $SnO_2$ , and  $WO_3$ . These nanostructured materials have been synthesized in a variety of different morphologies such as nanotubes, nanorods, nanowires, and nanocrystals, with the aim of amplifying dye adsorption and optimizing electron injection [39,40]. Among these materials,  $TiO_2$  nanoparticles stand out as the most promising candidate for DSSCs. Their exceptional transparency across the visible spectrum, remarkable stability, non-toxicity, and substantial specific surface area make them highly attractive for next-generation solar cells [41]. The standard  $TiO_2$  paste formulation includes organic binders and viscous solvents, which require a high-temperature sintering process (typically 400–500 °C) to establish effective electrical connectivity between particles. However, the high-temperature process becomes challenging when employing FPCSs, as they have limited thermal stability. Achieving low-temperature fabrication of the titania layer in DSSCs manufactured on FPCSs is a

crucial requirement since the low thermal stability of the substrate (approximately 150 °C) is a significant obstacle. To address these challenges, innovative strategies and techniques have been proposed to enable the deposition of TiO<sub>2</sub> layers at temperatures within the acceptable range for conducting polymers [19]. Consequently, this has spurred the scientific community to explore diverse methodologies, primarily focused on optimizing the properties of the TiO<sub>2</sub> paste and employing various pre- and post-treatment techniques to achieve high-efficiency flexible devices [42–44]. These techniques are further described in Section 5.

To prepare a screen-printable TiO<sub>2</sub> nanocrystalline paste without the need for the sintering process, several specific requirements must be fulfilled. Firstly, the paste needs to have sufficiently high viscosity in the absence of the generally used insulating binder materials. The presence of the binders in dried film can hinder carrier transport between TiO<sub>2</sub> particles [45]. Secondly, strong adhesion of the paste and film to the hydrophobic surface of ITO-coated PEN is of utmost importance. Furthermore, complete evaporation of all liquid constituents of the paste at temperatures below 150 °C is imperative [46]. Lastly, all components of the paste should exhibit inert characteristics to prevent any potential corrosion of the underlying ITO layer, for example, by avoiding the presence of acidic precursors, which in addition could undermine interparticle connections [47]. Another crucial aspect that warrants careful consideration is the use of ultrathin films (<6 μm). These thin films on FPCSs serve four purposes: (i) to minimize electron diffusion distances; (ii) to enhance mass transport by reducing the ionic diffusion distance; (iii) to improve adhesive properties between the paste and the substrate, as thicker films are prone to delamination; and (iv) to reduce the presence of macroscopic cracks [48]. In this regard, to ensure optimal performance of an ultra-thin-film F-DSSC, it is imperative to employ dyes with a high molar extinction coefficient, thus maximizing light absorption and, ultimately, improving device efficiency [49]. Hereinafter, F-DSSCs refer to DSSCs fabricated on FPCSs.

In the next section, the pioneering works, cutting-edge strategies and techniques for the fabrication of F-DSSCs are explained. These strategies have been developed in order to improve the interconnection between TiO<sub>2</sub> nanoparticles and can be applied at different stages of the fabrication process. Some techniques can be applied during TiO<sub>2</sub> synthesis and paste, colloid, or dispersion preparation. Other techniques are related to the photoanode preparation, such as the formation of the film using low-temperature deposition methods, film transfer, and film compression, and other strategies are applied to the last step, i.e., to the final deposited film as post-treatment.

## 5. Mastering Flexibility: Pioneer and Cutting-Edge Strategies for Photoelectrode Manufacturing

### 5.1. Low-Temperature Physical-Chemical Binding

The development of a surfactant-free paste is one of the most appealing alternatives. A low-temperature screen-printable TiO<sub>2</sub> paste poses a significant challenge in the fabrication of F-DSSCs. This crucial issue demands careful consideration and innovative approaches to overcome the difficulty and achieve successful manufacturing outcomes. In this regard, incorporation of a binding agent, using different sizes of TiO<sub>2</sub> nanoparticles, and/or surface modification of TiO<sub>2</sub> by stirring or ball-milling has been applied to obtain surfactant-free viscous pastes with interconnection between titania nanoparticles.

Binding agents such as TiCl<sub>4</sub> or [Ti(OiPr)<sub>4</sub>] mixed with commercial P25 have been used. Ti(IV) alkoxides can be hydrolyzed and crystallized inside the semiconductor oxide network at low temperatures, which serves to chemically interconnect the titania nanoparticles and to provide adhesion between the film and the substrate [50–52]. Another binder-free approach is using acid–base chemistry by adding a small amount of ammonia solution to acidic TiO<sub>2</sub> in order to change the pH and, hence, chemically sinter the film. An increase in CH<sub>3</sub>COO<sup>−</sup> and NH<sub>4</sub><sup>+</sup> ions concentration is responsible for flocculation acting as an “electrolyte glue” [30]. In fact, an increase in viscosity is due to the increase in connectivity between the particles during drying because of the formation of hydroxyl groups on the

TiO<sub>2</sub> surface [53,54]. Holliman et al. reported a low-temperature binder-free, aqueous paste using commercial Degussa P25 and hexafluorotitanic acid used as a binding agent to chemically sinter TiO<sub>2</sub> particles. By this approach, the interparticle connectivity was increased due to condensation protonation–dehydration reactions on the surface of the TiO<sub>2</sub> and, at the same time, forming Sn-O-Ti bonds between ITO substrate and TiO<sub>2</sub> [55]. Surface modification of TiO<sub>2</sub> nanoparticles using trimethyloxysilane is another approach that results in an increase in the crystallinity of TiO<sub>2</sub> nanoparticles, surface area, and porosity of the film. The modified TiO<sub>2</sub> showed a greater extent of dye loading in comparison with bare TiO<sub>2</sub> due to a better interaction between dye anchoring groups and Ti-O-Si bonds and with free -OH groups of TiO<sub>2</sub> nanoparticles [56].

Miyasaka et al. performed some of their earlier work on low-temperature binder-free coatings for F-DSSC electrodes (<130 °C) using a colloidal solution containing two different sizes of TiO<sub>2</sub> particles in water and *t*-butanol. The smaller particles with an average size of about 60 nm acted as a binding agent between nanoparticles and the larger particles with an average size of about 200 nm, which served as a light scattering material [47,57]. Also, other research groups have used a range of different particle sizes (small: medium: large) to fill the voids between the middle-sized TiO<sub>2</sub> particles and thus to bind particles together; the larger particles act as light scattering centers [58].

To obtain a homogeneous and viscous dispersion, researchers have mixed commercial P25 with Millipore water or dry ethanol and the effect of stirring for several weeks to change the surface chemistry of bare P25 [59]. Also, applying ball-milling to the titania slurries for several hours has resulted in small agglomerates, fewer cracks, and more homogeneous films. The ball-milled films exhibit high mechanical stability and an increase in dye loading due to an increase in the surface area [53,54,60].

## 5.2. Film Transfer Techniques

Owing to the absence of sintering in low-temperature films, which poses challenges in achieving effective particle interconnectivity, lift-off methods have emerged as a viable alternative to preserve particle connectivity. These methods involve initially sintering the material on a template and subsequently transferring it to an FPCS, ensuring the desired interparticle contacts.

Dürr et al. presented a lift-off technique in which a pre-sintered electrode is transferred to a second plastic substrate maintaining its original electrical properties. They prepared a thin gold layer (10–20 nm) on a glass substrate. On top of this, a high-temperature annealed (>450 °C) TiO<sub>2</sub> layer was deposited. This transfer layer consisted of a composite that comprises one sublayer of TiO<sub>2</sub> spheres in the lower part and one sublayer of TiO<sub>2</sub> rods in the upper part. This combination of morphologies enhances the mechanical properties resulting in an optimized lift-off process [61].

A laser processing technique has been used by Kafafi et al. to deposit mesoporous TiO<sub>2</sub> films onto ITO-PET substrates from a colloidal solution of commercial P25, water, acetylacetone, Triton X-100, and polyethylene glycol. A laser direct-write technique (LDW) was used to transfer a TiO<sub>2</sub> film deposited onto a borosilicate glass plate to an ITO-PET substrate [62,63]. Also, Huang et al. reported a laser-assisted lift-off combined with a roll pressure rolling process for the preparation of TiO<sub>2</sub> photoelectrodes on ITO-PET substrates, achieving an efficiency of 4.2% [64].

Another film-transfer approach was investigated by Ma et al. They obtained a TiO<sub>2</sub> film on a flexible ITO-PET substrate using friction transfer of a sintered TiO<sub>2</sub> layer. They sprayed a low-temperature dispersion of TiO<sub>2</sub> on the ITO-PET substrate and a sintered TiO<sub>2</sub> film coated on a ceramic tile by doctor blading. This sintered film was placed in face-to-face contact with the underlying TiO<sub>2</sub> layer on the ITO-PEN and moved across. In this way, the sintered layer was transferred from the ceramic tile to the surface of the bottom layer under the friction generated between the layers [65].

Although relatively good efficiencies have been achieved with this method, it is undeniable that translating this technique into a continuous production process is highly challenging.

### 5.3. $\text{TiO}_2$ Film Compression

In 2000, Hagfeldt and coworkers patented a method for fabricating a nanostructured film on FPCSs in a continuous fashion. They proposed an embodiment of an FPCS roll arranged to form a continuous web that undergoes motion toward a set of two pressure rollers. In its way, a colloidal suspension, in a receptacle, is deposited and evaporated before being compressed by the rollers. The compression applied to the film helps the disruption of large agglomerates resulting in a highly light scattering effect and increasing the specific surface area. The result is a mechanically stable, nanostructured, porous film that adheres well to the substrate. They examined the effect of compression applied to the porous layer by a planar steel press plate. They demonstrate that the porosity of the film decreases when the applied pressure increases. On the other hand, the internal surface area showed a slight increase from 60.6 to 63.9  $\text{m}^2/\text{g}$ . With respect to the BET pore size, the compressed films showed a more homogeneous pore size distribution ranging from 4–60 nm for unpressed powder and 30–40 nm for pressed films. The introduction of this automated method provides a significant advantage by allowing for a continuous roll-to-roll high-speed manufacturing process [31,66–70]. The same group developed a step-by-step baseline for the fabrication of F-DSSCs on ITO-PET. They reported one of the first F-DSSC modules for indoor environments obtaining a maximum power output of approximately 2.3  $\mu\text{W}/\text{cm}^2$  at 250 lux using fluorescent light [29].

After this breakthrough, many research groups have focused on the improvement of this technique by optimizing experimental parameters such as applied pressure [42]. By varying the pressure, the microstructure of the  $\text{TiO}_2$  films is changed, and the interparticle connection is improved, resulting in higher photon-induced charge transport and slower recombination kinetics [71]. As a result, the electron transport resistance decreased with an increase in applied pressure. A more compact  $\text{TiO}_2$  film structure results in rapid electron transport and a reduction in back recombination, which enhances the  $J_{\text{SC}}$  [72–74].

Regarding the compression technique, Cheng et al. presented the potential use of a cold isostatic pressure (CIP) technique for the preparation of high-quality  $\text{TiO}_2$  flexible electrodes. A 30 wt% titania suspension using P25 and ethanol was prepared and coated by the doctor blade technique onto ITO-PET. The films were transferred to a polyethylene envelope and sealed under vacuum ( $10^{-1}$  Torr) and subsequently compressed with a CIP instrument. The films showed a strong bond between particles and presented a uniform free-crack surface morphology, which indicates good interparticle connectivity [48].

### 5.4. Low-Temperature Deposition Techniques

The commonly used low-temperature deposition techniques are blade coating (doctor blading), screen printing, spin coating, spray coating, slot-die, and inkjet printing. Each technique has advantages and disadvantages, and the printing parameters must be adjusted in order to achieve homogeneous crack-free films. As mentioned previously, the main issue related to these methods is the preparation of binder-free colloids, pastes, or dispersing media, which directly affects the uniform and complete covering of the substrate followed by film adhesion to the substrate.

Among low-temperature deposition techniques, electrophoretic deposition (EPD) has received attention due to several advantages, enabling uniform and controlled deposition of particles. The major advantage of EPD is that it can be performed at low temperature, making it suitable for coating ITO-PEN substrates without causing damage. EPD is a technique that has great potential for processing low-temperature films [75–77]. However, there are some limitations that make it less suitable for large-scale production of thin films. EPD typically involves a slow deposition process, which can hinder the efficiency and speed required for large-scale production. Coating a large area with EPD can be

time-consuming. In addition, achieving uniformity and consistency at a large scale can be technically complex.

In the pursuit of techniques that can be adapted to these processes, multiple strategies have been developed to further enhance the interconnection between TiO<sub>2</sub> nanoparticles and adhesion with the substrate. In the following, the most relevant post-treatments on low-temperature films are presented [78–82].

#### 5.5. UV Irradiation Post-Treatment

UV radiation has been used to further enhance the interconnection between TiO<sub>2</sub> particles and improve film homogeneity. In this post-treatment, a precursor is commonly employed in the preparation of the colloidal solution, which when irradiated by UV promotes improved interparticle connectivity within the film. UV irradiation is also a suitable method for removing organic and inorganic residues from the TiO<sub>2</sub> film, which originate from the suspension during the synthesis process [83–89]. However, care must be taken when using this method since exposing TiO<sub>2</sub> films to UV can affect adherence to the substrate and adsorption of the dye sensitizer. FTIR spectroscopy and SEM are helpful methods to demonstrate if the organic impurities on the TiO<sub>2</sub> surface are eliminated or not without modifying the morphology of the film. In addition, UV treatment may enhance the dye loading on the films [84]. Ayllón et al. explored the use of UV irradiation to prepare low-temperature TiO<sub>2</sub> photoelectrodes for FPCSs. They proposed an alternative method to prepare porous TiO<sub>2</sub> thick films. In this approach, they made use of a soluble precursor of TiO<sub>2</sub> that undergoes photodegradation, promoting the formation of necks between particles and enhancing adherence to the substrate. They prepared a colloidal solution by mixing commercial P25, titanium(IV) bis(ammonium lactate)dihydroxide (TALH), Triton-X, and water, assisted by an ultrasonic bath. The photodegradation of TALH promotes the formation of small TiO<sub>2</sub> particles that act as cement to electrical connections among bigger particles. After the deposition onto an ITO-PET substrate by doctor blading, the film was UV irradiated at 80 °C for 6 h using a medium-pressure Hg Lamp. The organic nature of this precursor allows its removal after UV irradiation [86].

#### 5.6. Microwave Irradiation Post-Treatment

A technique that holds great potential for the manufacturing of solar cells using FPCSs is microwave treatment. Through this post-treatment, it is possible to achieve a substantial increase in the local temperature within the film, facilitating the sintering process without damaging the FPCS. This post-treatment results in promoting the electrical interconnections between TiO<sub>2</sub> nanoparticles and, hence, an improvement in photovoltage, current density, and efficiency [90–93].

#### 5.7. Accelerated Electron Beam (EB) Post-Treatment

Another low-temperature (50 °C) post-treatment technique for FPCSs is an accelerated electron beam (EB). In this technique, the accelerating voltage is adjusted to control the penetration depth of the electron into the TiO<sub>2</sub> film in order to achieve particle necking without damaging the FPCS. Yamaguchi et al. prepared a binder-free paste by grinding a mixture of commercial TiO<sub>2</sub> P25, water, and ethyl alcohol and deposited it by doctor blading onto an ITO-PET substrate. The film was exposed to the EB, and the DSSCs fabricated reached an efficiency of 2.1%. Using this method, they show that TiO<sub>2</sub> particle necking was successfully achieved at room temperature [94].

#### 5.8. Combination of Different Strategies

Various research groups have shown that the combination of different strategies will result in a significant performance improvement of F-DSSCs. Yamaguchi et al. reported a combined press method with the use of a TiO<sub>2</sub>-water-based paste and a UV-O<sub>3</sub> surface treatment before and after paste deposition. They used two different TiO<sub>2</sub> particle sizes in the paste of a weight ratio of 7:3, 20, and 100 nm, respectively. The mechanical adhesion

strength of TiO<sub>2</sub> nanoparticles to the substrate was measured by ISO/DIS 15814 [95] methods showing a strong adherence [96]. An efficiency of 8.1% was obtained in an F-DSSC using this method, and by placing an anti-reflecting film on the outer surface of the DSSC reaching a certified power conversion efficiency of 7.6% by the RCPV, AIST, in Japan [96,97].

Zaban et al. explored an approach to produce an improved TiO<sub>2</sub> nanoporous electrode on FPCSs by studying the combined effect of electrophoretic deposition of colloidal commercial P25 with the mechanical compression method applying non-polar volatile organic liquids to fill the pores of dry TiO<sub>2</sub> films [98]. Huan Yang et al. reported the fabrication of laser-sintered TiO<sub>2</sub> electrodes for F-DSSC. A binder-free paste was prepared by mixing commercial P25 Degussa and ethanol. The photoelectrode was prepared by paste deposition using a doctor blade technique onto an ITO-PEN substrate and a subsequent compression of the film (200 MPa for 30 s) in a cold isostatic pressing machine. IR laser sintering (1065 nm) was used to promote a uniform local sintering (550 °C) of the film without damaging the FPCS. This helped to form necking connections between TiO<sub>2</sub> nanoparticles and a transformation from anatase to rutile phase in part of the nanomaterial. These strategies enhanced the charge collection efficiency, the absorption of incident light, and an increase in efficiency from 4.6% to 5.7%, showing a potential application of this method for the roll-to-roll production of F-DSSC [73].

Also, the deposition of a blocking compact layer in order to hinder the recombination process is reported by different groups [99,100]. The low-temperature compact TiO<sub>x</sub> on the ITO surface or Al<sub>2</sub>O<sub>3</sub> electron recombination blocking layer on a TiO<sub>2</sub> film not only suppresses interfacial charge recombination between injected electrons and dye cations, but also enhances the adhesion between ITO-PEN and the TiO<sub>2</sub> film [49,101].

Miyasaka and coworkers explored one of the first investigations on the co-sensitization effect of TiO<sub>2</sub> films to improve F-DSSC efficiency. They deposited a commercial binder-free TiO<sub>2</sub> paste (PECC-K01) on an ITO-PEN substrate with a subsequent heat-drying treatment at 150 °C for 10 min. They made use of different dyes (FL, N719, and black dye) in order to broaden the absorption spectrum. By improving the immersion time in the different dye baths, they obtained a co-sensitized F-DSSC with an efficiency of 5.10% [102].

Another interesting low-temperature approach (<200 °C) was reported by Kunzmann et al. They integrated the Ru(II)-based N3 dye into the anatase TiO<sub>2</sub> network. The pastes were prepared by dispersing the powders in absolute ethanol (EtOH). They showed that the integrated network layer contributes to enhancing the device stability by improving resistance to electron recombination in TiO<sub>2</sub> with the electrolyte. In addition to a top integrated network layer, they used a bottom layer consisting of a P25:TiO<sub>2</sub>-sp mixture (80:20) to maximize the short-circuit current density and collection yields. They reported multilayered photoelectrode devices with an efficiency of 8.75% that are stable up to 600 h under operation conditions [46].

Kim et al. prepared an efficient, flexible, organic dye-based DSSC using a cobalt-based redox electrolyte. They prepared a hierarchically structured TiO<sub>2</sub> film (HS-TiO<sub>2</sub>) on a flexible ITO-PEN substrate, using a high molar extinction coefficient organic dye (JH-1) ( $\epsilon = 50,000 \text{ M}^{-1}\text{cm}^{-1}$ ). A 10% (wt/v) commercial P25 powder in an ethanol solution was directly electro-sprayed onto the FPCS. After this, compression (10 MPa) was applied to the film for 10 min. With this configuration, they obtained an efficiency of 6.12% by optimizing the thickness of the HS-TiO<sub>2</sub> photoelectrode [103,104].

Table 1 provides a summarized compilation of critical parameters utilized in pioneering work on the development of F-DSSCs.

**Table 1.** Pioneering work in the fabrication process of F-DSSCs.

Substrate Type	Applied T (°C)/Time (h)	Strategy Applied to the Low-T Films	Deposition Method	Active Layer Compositions	Thickness (μm)	Dye	Electrolyte	Counter Electrode	PCE (%) at 1 Sun	Ref.
ITO-PET	100/12	Laser direct-write technique	-	Colloidal TiO <sub>2</sub> paste of P25, Degussa), water, acetylacetone, Triton X-100, PEG	12	N3	I <sup>-</sup> /I <sub>3</sub> <sup>-</sup> -based	E-beam-evaporated-pt	0.71	[62,63]
FTO glass	100/24	-	Spin coating	Synthesized colloidal TiO <sub>2</sub> solution	1	N3	I <sup>-</sup> /I <sub>3</sub> <sup>-</sup> -based	Pt-coated FTO glass	1.22	[105]
ITO-PET	Room T	Compression by rollers	Doctor blade	P25, ethanol	8	N719	I <sup>-</sup> /I <sub>3</sub> <sup>-</sup> -based	Porous carbon and porous platinized	2.3	[66–69]
ITO-PET	Room T	Compression	Doctor blade	P25, ethanol	12	Black and red dye	I <sup>-</sup> /I <sub>3</sub> <sup>-</sup> -based	Platinized SnO <sub>2</sub> powder pressed on ITO-PET	5.5	[70]
ITO-PET	Room T	Compression (adjusting the pressure and thickness of the deposited layer)	Doctor blade	P25, ethanol or water	-	N719	I <sup>-</sup> /I <sub>3</sub> <sup>-</sup> -based	Platinized Sb-doped SnO <sub>2</sub>	2–3 (6.1% at 0.1 sun)	[29]
PET-ITO	<80	UV irradiation	Doctor blade	P25, TALH solution, Triton X-100, water	12	N3	I <sup>-</sup> /I <sub>3</sub> <sup>-</sup> -based	Pt-coated FTO glass	2%	[86]
PET-ITO	130/4	UV irradiation	Doctor blade	commercial TiO <sub>2</sub> suspension (Solaronix)	-	N719	Polymer electrolyte	Sputtered Pt on PET-ITO	0.23	[84]

Table 1. Cont.

Substrate Type	Applied T (°C)/Time (h)	Strategy Applied to the Low-T Films	Deposition Method	Active Layer Compositions	Thickness (μm)	Dye	Electrolyte	Counter Electrode	PCE (%) at 1 Sun	Ref.
ITO-PET	-	Compression using stainless-steel plates and using Al <sub>2</sub> O <sub>3</sub> electron recombination blocking layer	Doctor blade	P25, dry ethanol	8	Ru-based	Polymer electrolyte	Sputtered Pt on ITO-PET	2.5 (5.3% at 0.1 sun)	[101]
ITO-PET	50	Accelerating electron-beam (EB) shower	Doctor blade	TiO <sub>2</sub> paste of P25 in ethyl alcohol	10	N3	I <sup>-</sup> /I <sub>3</sub> <sup>-</sup> -based	Pt-coated FTO glass	2.1	[94]
ITO-PET	80/20	Chemical vapor deposition + UV irradiation + microwave irradiation	Electrophoretic deposition	Commercial TiO <sub>2</sub> (F-5), tert-butyl alcohol, acetonitrile	10	Ru-based	I <sup>-</sup> /I <sub>3</sub> <sup>-</sup> -based	Pt-coated FTO glass	3.8	[91,92]
FTO glass	100/12	Hydrothermal crystallization of TiCl <sub>4</sub> as a chemical glue	Doctor blading	Commercial P25, TiCl <sub>4</sub>	10	Ru-based	I <sup>-</sup> /I <sub>3</sub> <sup>-</sup> -based	Pt-coated FTO glass	6.23	[50]
ITO-PET	-	Multi-mode microwave heating	Spray coating	Slurry of synthesized TiO <sub>2</sub> nanoparticles	60	Ru-based	I <sup>-</sup> /I <sub>3</sub> <sup>-</sup> -based	Pt-coated FTO glass	2.16	[93]
ITO-PET	Room T	Laser-assisted lift-off combined with a roll-pressing process	Mechanical pressing and transferring	Sintered TiO <sub>2</sub> tape	14	N719	-	Hydrolysis Pt counter electrode	4.2	[64]
ITO-PET	Room T	In situ hydrolysis using TTIP, UV ozone treatment	Doctor blade	P25, TTIP, ethanol	8	N3	I <sup>-</sup> /I <sub>3</sub> <sup>-</sup> -based	Platinized ITO-PET	3.27	[106]

Table 1. Cont.

Substrate Type	Applied T (°C)/Time (h)	Strategy Applied to the Low-T Films	Deposition Method	Active Layer Compositions	Thickness (μm)	Dye	Electrolyte	Counter Electrode	PCE (%) at 1 Sun	Ref.
FTO	150/0.25	Acid–base chemistry	Doctor blade	Synthesized TiO <sub>2</sub> particles, ammonia solution	4.3	N719	I <sup>−</sup> /I <sub>3</sub> <sup>−</sup> -based	Pt-coated FTO	2.55	[30]
ITO-PEN	<150	Using binding agent (HCl)	Doctor blade or screen printing	Colloidal solution of TiO <sub>2</sub> with different particle sizes	10	N719	I <sup>−</sup> /I <sub>3</sub> <sup>−</sup> -based with different solvents	Pt-coated FTO glass	5.8 (6.4% at 0.23 sun)	[47]
ITO-PEN	130	Surface treatment of ITO using sputtered TiO <sub>x</sub> layer as a buffer layer followed by anodization	Doctor blade	Commercial binder-free paste (Pecell)	12	D149	I <sup>−</sup> /I <sub>3</sub> <sup>−</sup> -based	Pt-coated FTO glass	3.7	[99]
ITO-PEN	<150	Sputtered TiO <sub>x</sub> layer as a buffer layer followed by anodization, and using co-adsorbent	Doctor blade	Synthesized TiO <sub>2</sub> nanoparticles with different sizes, tert-butanol, water	10	N719, SJW-E1	I <sup>−</sup> /I <sub>3</sub> <sup>−</sup> -based with different solvents	Pt-sputtered FTO glass	6.31	[100]
ITO-PEN	150	TiO <sub>x</sub> compact blocking layer	Doctor blade	Binder-free TiO <sub>2</sub> paste	3.5	D205	I <sup>−</sup> /I <sub>3</sub> <sup>−</sup> -based	Pt-sputtered FTO glass	5.2	[49]
ITO-PET	Air drying	Surface-modified TiO <sub>2</sub> nanoparticles	Doctor blade	Synthesized TiO <sub>2</sub> nanoparticles, methyl glycine, trimethoxy silane, toluene	33	N749 and N719	I <sup>−</sup> /I <sub>3</sub> <sup>−</sup> -based and Co-based	Platinum coated	4.1	[56]
ITO-PET	120	Condensation protonation–dehydration reaction using H <sub>2</sub> TiF <sub>6</sub> as a binding agent to chemically sinter the TiO <sub>2</sub> particles	Doctor blade	P25, H <sub>2</sub> TiF <sub>6</sub> , water	-	N719 and SQ1	I <sup>−</sup> /I <sub>3</sub> <sup>−</sup> -based	Pt-coated	4.2	[55]

Table 1. Cont.

Substrate Type	Applied T (°C)/Time (h)	Strategy Applied to the Low-T Films	Deposition Method	Active Layer Compositions	Thickness (μm)	Dye	Electrolyte	Counter Electrode	PCE (%) at 1 Sun	Ref.
ITO-PEN	120/0.25	Cold isostatic pressing (CIP)+ laser sintering	Doctor blade	P25, ethanol followed by ball-milling	13	N719	I <sup>-</sup> /I <sub>3</sub> <sup>-</sup> -based	Pt-coated ITO-PEN	5.7	[73]
ITO-PEN	150	Combination of compression method and light confining effect of TiO <sub>2</sub> -water paste	Doctor blade	Paste of TiO <sub>2</sub> nanoparticles with different sizes and ethanol	4–8	N719	I <sup>-</sup> /I <sub>3</sub> <sup>-</sup> -based	Pt-sputtered ITO-PEN	7.4	[48]
ITO-PEN	Room T	Compression method	Doctor blade	Paste of TiO <sub>2</sub> nanoparticles with two different sizes and ethanol	6–10	N719	I <sup>-</sup> /I <sub>3</sub> <sup>-</sup> -based	Pt-sputtered ITO-PEN or Ti foil	7.6	[97]
ITO-PET	200	Lift-off technique + compression method	Transfer process	TiO <sub>2</sub> nanosphere and nanorods	8–10	Ru-based	Polymer gel based on I <sup>-</sup> /I <sub>3</sub> <sup>-</sup>	Pt-evaporated ITO-PET	5.8	[61]
ITO-PET	150	Post-treatment with TiO <sub>2</sub> sol	Electrophoretic deposition	Commercial TiO <sub>2</sub> (F-5 and G-2), t-butyl alcohol, acetonitrile	5–20	N719	I <sup>-</sup> /I <sub>3</sub> <sup>-</sup> -based	FTO glass	4.1 (4.3% at 0.23 sun)	[77]
ITO-PEN	150/0.5	Ball milling	Doctor blade or spin coating	P25, ethanol	1–16	N719	I <sup>-</sup> /I <sub>3</sub> <sup>-</sup> -based	Pt-coated ITO-PEN	4.2	[60]
ITO-PEN	150/0.5	Ball milling + chemically modification of slurry with HCl	Doctor blade	P25, ethanol	8	N719	I <sup>-</sup> /I <sub>3</sub> <sup>-</sup> -based	Pt-coated ITO-PEN	5.0	[53]
ITO-PEN	150/0.5	Ball milling + chemically modification of slurry with HCl and ammonia	Doctor blade	P25, ethanol	10.3	N719	I <sup>-</sup> /I <sub>3</sub> <sup>-</sup> -based	Pt-coated ITO-PEN	4.9	[54]

Table 1. Cont.

Substrate Type	Applied T (°C)/Time (h)	Strategy Applied to the Low-T Films	Deposition Method	Active Layer Compositions	Thickness (μm)	Dye	Electrolyte	Counter Electrode	PCE (%) at 1 Sun	Ref.
ITO-PET	Air drying	Cold isostatic pressure (CIP)	Doctor blade	Commercial P25	17.5	N719	I <sup>-</sup> /I <sub>3</sub> <sup>-</sup> -based	Pt-coated ITO-PEN	6.3 (7.4% at 0.15 sun)	[48]
ITO-PEN	100/2	UV irradiation and heat treatment	Spin coating	P25, acetylacetone, water, triton X-100	10–15	N3, N719	I <sup>-</sup> /I <sub>3</sub> <sup>-</sup> -based liquid electrolyte and solid electrolyte based on polysaccharide	Pt-coated ITO-PEN	2.63	[87]
ITO-PEN	150	Low-temperature chemical sintering of the graded film	doctor blade	P25 and TiO <sub>2</sub> (12, 28, and 100 nm)	3–4	K-N719	I <sup>-</sup> /I <sub>3</sub> <sup>-</sup> -based	Pt-coated FTO glass	3.05	[58]
ITO-PET	100/30	Alkoxide hydrolysis of TIIP, resulting in an interconnection between the particles	Dip coating	Nanocrystalline colloid of titanium isopropoxide (TIIP) in an ethanolic dispersion of commercial P25	2	Ru-based	Synthesized gel electrolyte based on I <sup>-</sup> /I <sub>3</sub> <sup>-</sup>	Platinized ITO-PET	3.2 (3.4% at 0.125 sun)	[52]
ITO-PET	-	Direct UV irradiation of the oxide nanoparticles and using light scattering particles	Coating with a glass rod	Synthesized TiO <sub>2</sub> , pentan-2,4-dione, Triton X-100, water	1.1 and 2.3	N3	I <sup>-</sup> /I <sub>3</sub> <sup>-</sup> -based	Pt-coated FTO glass	2.5	[89]
ITO-PEN	125/1	Friction-transfer technique + compression method	Spray coating	Paste of P25, TBT, ethanol	28	N719	I <sup>-</sup> /I <sub>3</sub> <sup>-</sup> -based	Pt-coated ITO-PEN	5.7	[65]

Table 1. Cont.

Substrate Type	Applied T (°C)/Time (h)	Strategy Applied to the Low-T Films	Deposition Method	Active Layer Compositions	Thickness (μm)	Dye	Electrolyte	Counter Electrode	PCE (%) at 1 Sun	Ref.
ITO-PEN	150	Using smaller particles for interconnection between bigger particles	Doctor blade	Paste of TiO <sub>2</sub> nanoparticles (9, 23, and 60 nm)	5–6	KN-719	I <sup>-</sup> /I <sub>3</sub> <sup>-</sup> -based	Platinized ITO glass	3.93	[71]
ITO-PEN	Air drying	Compression method	Doctor blade	Paste TiO <sub>2</sub> nanoparticles with different sizes	6–12	N719	I <sup>-</sup> /I <sub>3</sub> <sup>-</sup> -based	Pt-coated ITO-PEN	4.21	[72]
ITO-PEN	150/0.16	-	Doctor blade	commercial binder-free TiO <sub>2</sub> paste (Pecell)	10	co-sensitization FL and N719, FL and black dye	I <sup>-</sup> /I <sub>3</sub> <sup>-</sup> -based	Pt-sputtered FTO glass	5.10	[102]
ITO-PEN	140/0.5	Compression	Doctor blade	binder-free colloidal suspension of commercial P25	-	N719	I <sup>-</sup> /I <sub>3</sub> <sup>-</sup> -based	Pt-coated ITO-PEN	4.39	[42]
ITO-PEN	Room T	Resonant multiple light scattering effect	Electrospray coating	Hierarchically structured TiO <sub>2</sub> and P25	3–12	JH-1	Co-based	Pt-Ti-sputtered ITO-PEN	6.12	[104]
ITO-PEN	120	Using binding agent H <sub>2</sub> TiF <sub>6</sub> to interconnect the particles	Doctor blade	Homemade TiO <sub>2</sub> nanoparticles, H <sub>2</sub> TiF <sub>6</sub> , water	6.4	N719	I <sup>-</sup> /I <sub>3</sub> <sup>-</sup> based with different solvents	PEDOT-coated ITO-PEN	1.0	This work

## 6. Experimental Section

In the following, key processes for manufacturing DSSCs on rigid and flexible substrates using low-temperature methods are categorized into 7 subsections. In each section, materials and methods are explained in detail.

### 6.1. Rigid and Flexible Substrates Preparation

In this work, ITO-coated glass (2 cm × 2 cm, <10 Ω/□, 1.1 mm thickness, XOP Glass, Castelló, Spain) was used for the photo and counter electrodes for rigid DSSCs. ITO-PEN substrates (cut from 297 mm × 210 mm sheets, <10 Ω/□, 125 μm thickness, Peccel) were used for both electrodes for F-DSSCs. All substrates were cleaned using Alkonox<sup>®</sup> detergent, deionized water (DIW), ethanol, and isopropanol in an ultrasonic bath for 15 min in each stage and air dried before use. In the case of the counter electrodes, two holes were drilled in every substrate using a tungsten carbide drill tip before cleaning.

### 6.2. Low-Temperature Blocking Layer

In order to prepare a blocking layer onto the ITO substrates, 5 mL titanium diisopropoxide bis(acetylacetonate) (75% wt.% in isopropanol, Sigma-Aldrich, Burlington, MA, USA) was dissolved in 50 mL 2-propanol (anhydrous, 99.5%, Sigma-Aldrich) under a nitrogen environment. Rigid and FPCSs were masked and sprayed with this solution at 120 °C on a hot plate; 30 spray steps were employed with an interval of 1 min between every application. Finally, the substrates were left at 120 °C for 30 min.

### 6.3. TiO<sub>2</sub> Nanoparticle Synthesis

TiO<sub>2</sub> nanoparticles were synthesized by preparing a sol–gel solution with a subsequent hydrothermal treatment as follows: 4.04 mL glacial acetic acid (ACS reagent, ≥99.7%, Sigma-Aldrich) was added to 21.22 mL titanium (IV) isopropoxide (97%, Sigma-Aldrich) with stirring, and was left to stir for 15 min. The mixture was then added dropwise to 145 mL DIW with stirring. The colloidal solution was stirred for 1 h before adding 1.4 mL nitric acid (ASC reagent, 70%) as a peptizing agent. The sol–gel reaction mixture was heated from 25 °C to 80 °C at a rate of 1.5 °C/s, and was then held under reflux conditions at this temperature for 1 h and 40 min. Finally, the resulting transparent blueish dispersion was left to stir overnight. For the next step, 30 mL TiO<sub>2</sub> sol–gel precursor solution was added to a 45 mL Teflon-lined autoclave (Parr Instruments), and a subsequent hydrothermal treatment at 200 °C for 24 h was applied in a furnace. The resulting slurry was then washed with ethanol followed by separation through centrifugation at 4500 RPM for 10 min (ST8 Benchtop Thermo Scientific Centrifuge, China, Langensfeld, Germany) to remove the excess organic compounds in the solution derived from the acids used. This washing method was applied 3 times and the resulting viscous compact TiO<sub>2</sub> mass was dried at ambient temperature. A light yellowish powder was obtained after fine grinding of the TiO<sub>2</sub> nanomaterial in a mortar. This is indicative that some organic compounds may still be present. Two different post-cleaning treatments were applied to further clean the TiO<sub>2</sub> nanomaterial: (i) a heat treatment at 450 °C for 2 h, and (ii) UV irradiation for 10 min (Oriel UV lamp 6035, 90% 253.5 nm).

### 6.4. Binder-Free Aqueous Paste for Low-Temperature Rigid and Flexible Dye-Sensitized TiO<sub>2</sub> Films

The deposition solution was prepared as follows: first, 23.25 μL hexafluorotitanic acid solution (H<sub>2</sub>TiF<sub>6</sub>, 60 wt.% in H<sub>2</sub>O, 99.9% trace metals basis, Sigma-Aldrich) was added as an interparticle binding agent to 2.47 mL DIW with stirring, as described by Holliman et al. [55]. Then, 0.75 g synthesized TiO<sub>2</sub> powder was gradually added to this solution, alternating with stirring and ultrasonic bath treatment (Branson 2800, Kukje, USA) in order to break large agglomerates and to assure a well-dispersed solution. A highly viscous paste was obtained (pH = 2). The paste was deposited by doctor blading onto rigid and FPCSs using Kapton<sup>®</sup> tape (30 μm thickness) as a spacer on top of the blocking layer (Figure 3a). The active area of the films was 0.5 cm<sup>2</sup>. Films were heated to

120 °C for 15 min to promote interparticle connectivity and adhesion to the substrate. The low-temperature TiO<sub>2</sub> films presented strong adhesion to both substrates, and the FPCs could be bent without detachment of the films (Figure 3c). After the low-temperature annealing step, the TiO<sub>2</sub> films were immersed at 120 °C for 18 h in a 0.5 mM dye solution of cis-diisothiocyanato-bis(2,2'-bipyridyl-4,4'-dicarboxylato) ruthenium (II) bis(tetrabutylammonium N719 dye (Ruthenizer 535-bisTBA, Solaronix, Aubonne, Switzerland) in 1:1 *v/v* acetonitrile/tert-butyl alcohol (ACS reagent, ≥99.0%, Sigma-Aldrich).

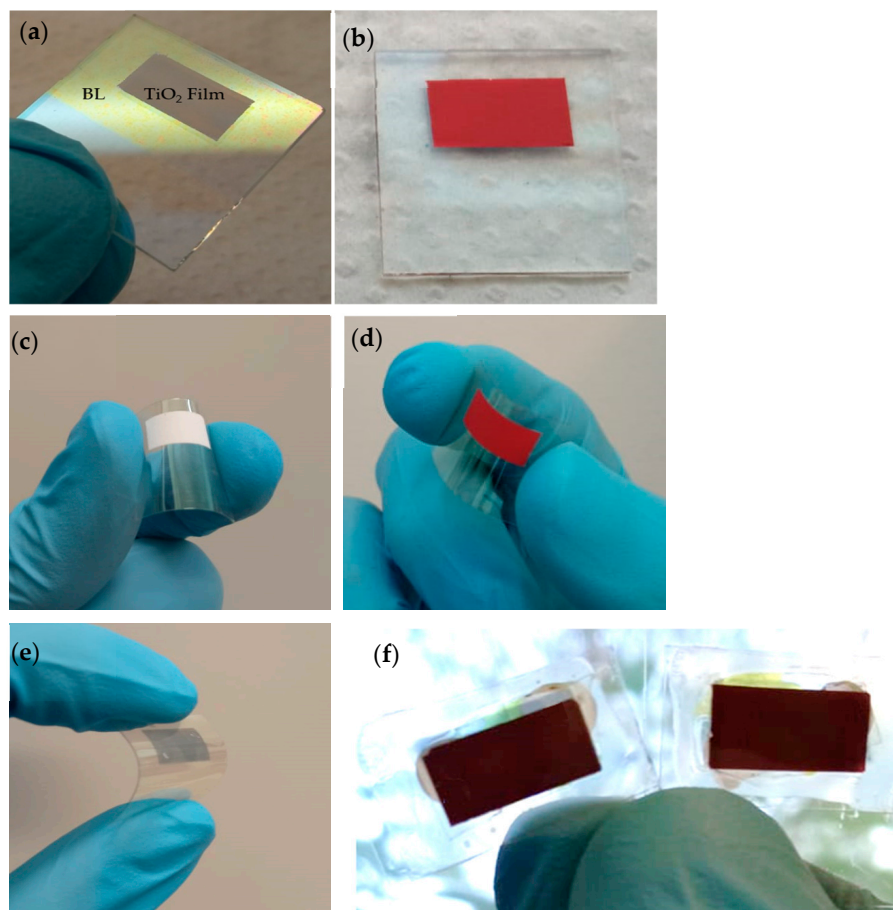


**Figure 3.** (a) TiO<sub>2</sub> film deposited on the low-temperature blocking layer (BL) (yellowish area); (b) dye-sensitized TiO<sub>2</sub> film after 18 h in the dye solution; (c) TiO<sub>2</sub> film deposited on an ITO-coated PEN substrate; (d) flexible dye-sensitized TiO<sub>2</sub> film; (e) flexible PEDOT counter electrode; (f) F-DSSCs.

### 6.5. Rigid and Flexible Counter Electrodes

For the fabrication of the counter electrodes, a solution was prepared of 0.1 M sodium dodecyl sulfate (ReagentPlus<sup>®</sup>, ≥98.5%, Sigma-Aldrich) and 0.01 M EDOT (3,4-ethylenedioxythiophene, 97%, Sigma-Aldrich) in DIW. Electropolymerization of poly(3,4-ethylenedioxythiophene) (PEDOT) on the conductive substrates was performed by using a Gamry potentiostat using a two-electrode configuration and applying a stationary voltage of 2.3 V for 120 s. The same substrate type (glass or PEN) was used as the counter electrode with an area two times larger than the working electrode.

### 6.6. Electrolyte Preparation

Three different redox electrolyte solutions were prepared: (i) ACN:VN; (ii) VA:ACN; and (iii) MN.

ACN:VN was prepared using 85:15 *v/v* acetonitrile/valeronitrile (99.5%, Sigma-Aldrich) with 0.1 M LiI (99.9% trace metal basis, Sigma-Aldrich), 0.05 M I<sub>2</sub> (ACS reagent, ≥99.8%, Sigma-Aldrich), 0.1 M 1,2-dimethyl-3-propylimidazolium iodide (DMPII, Solaronix), 0.6 M

guanidine thiocyanate ( $\geq 97\%$  titration, Sigma-Aldrich) and 0.5 M 4,4'-di-tert-butyl-2,2'-dipyridyl (98% Sigma-Aldrich). VA:ACN uses the same compounds as ACN:VN except these are dissolved in 15:85 *v/v* acetonitrile/valeronitrile. MN was prepared using 0.1 M  $I_2$ , 0.1 M LiI, and 0.8 M DMPII dissolved in 3-methoxypropionitrile ( $\geq 98.0\%$ , Sigma-Aldrich).

### 6.7. Rigid and F-DSSC Assembly

A UV-curable resin (Threebond<sup>®</sup> 3035B, Threebond International, Inc., West Chester Township, OH, USA) was deposited with an automatic UV-glue three-axis motion dispensing machine on both rigid and FPCS. The photo and counter electrodes were then attached in a sandwich configuration using clamps and exposed to UV irradiation (UVP UVGL-55 254/365 nm, Analytik Jena, Upland, CA, USA) to cure and seal the cells. The redox electrolyte solution was injected through the predrilled holes in the counter electrode, and then sealed again using the resin. F-DSSCs were fabricated using the best optimum configuration obtained from rigid devices. The fabricated rigid and F-DSSCs were characterized both at high and low light intensities.

## 7. Results

### 7.1. FT-IR Powder Measurements

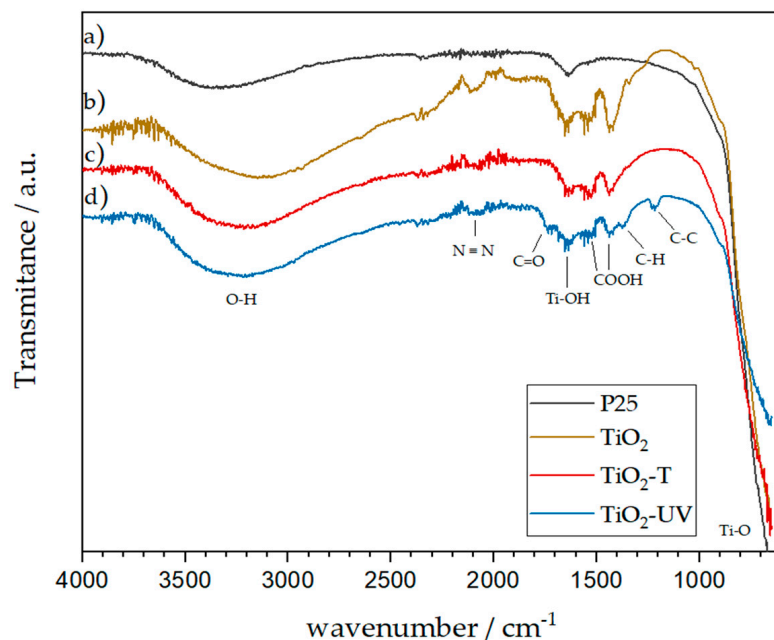
The identification of molecular absorption and functional groups on synthesized  $TiO_2$  surface was analyzed using an Agilent Cary 630 FTIR spectrometer, both with and without a post-cleaning treatment. Figure 4a shows the FT-IR spectrum of commercial P25  $TiO_2$  without further modification or processing. The typical absorption band at 450–615  $cm^{-1}$  corresponds to the presence of Ti-O metal oxide bonding. These bands for all samples are only indicated in Figure 4 (bottom right) due to limitations within the measurement range of the equipment. A common functional group was observed in all samples at 3000–3600  $cm^{-1}$  due to the presence of hydroxyl moieties (O-H) [107]. In addition, the absorption band in all samples at 1620  $cm^{-1}$  corresponds to the bending vibration of the Ti-OH bonds [108]. Figure 4b shows the FT-IR spectrum of synthesized  $TiO_2$  nanoparticles without any post-cleaning treatment. The presence of absorption bands between 1300 and 2150  $cm^{-1}$  reveals the presence of organic material on the surface of the  $TiO_2$  nanoparticles. Absorption bands at 1450 and 1530  $cm^{-1}$  are attributed to the symmetric and asymmetric stretching of carboxylate groups (-COOH), respectively [109]. Moreover, synthesized  $TiO_2$  nanoparticles show the presence of  $^-N=N^+=N^-$  with a peak at 2100  $cm^{-1}$ , suggesting an incomplete reaction during the sol-gel process. It can be inferred that nitrogen from nitric acid partially reacts and remains attached to the particle surface even after the cleaning process [110]. Following the post-cleaning processes, i.e., heat-treated synthesized  $TiO_2$  (Figure 4c) and UV-irradiated synthesized  $TiO_2$  (Figure 4d), these absorption bands can still be observed. However, the signals are significantly weaker compared to the non-treated sample. This strongly indicates that the cleaning process successfully achieves a reduction in the amount of contaminants on the surface of  $TiO_2$ . Samples exposed to UV irradiation (Figure 4d) presented the lowest degree of organic compounds in the same region compared to non-treated samples and heat-treated samples. However, additional absorption bands typical of the C-C vibration, alkene rocking structure (C-H), and carbonyl groups (C=O) can be observed at 1230  $cm^{-1}$ , 1360  $cm^{-1}$ , and 1742  $cm^{-1}$  respectively. This is attributed to UV-irradiation-induced reactions taking place among the remaining organic compounds on the  $TiO_2$  surface [107,109].

### 7.2. XRD Characterization $TiO_2$ Nanomaterial

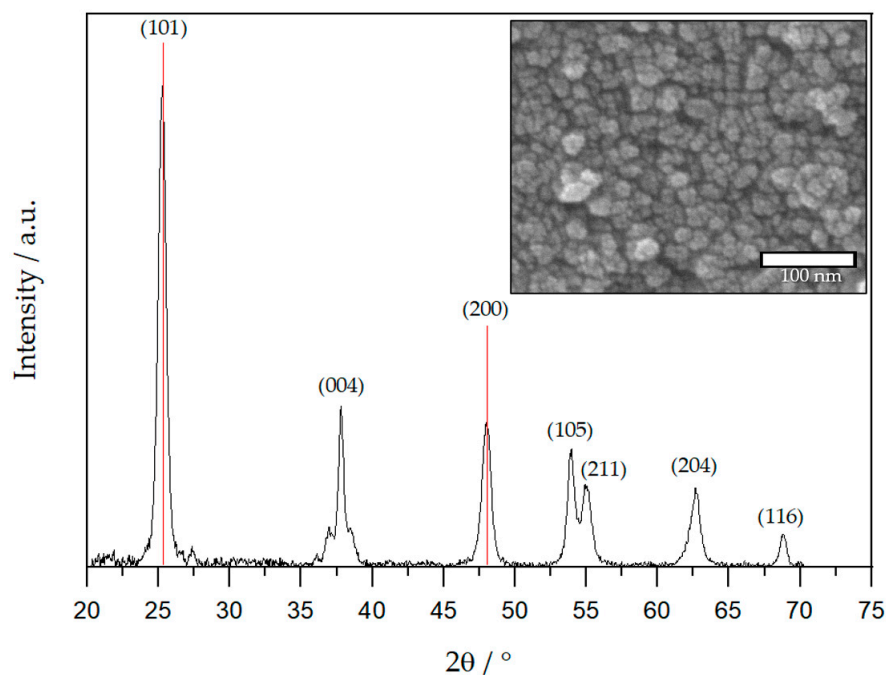
A Bruker D8 ADVANCE X-ray diffractometer was used to characterize the prepared  $TiO_2$  nanomaterials. Figure 5 shows that the XRD peaks of the synthesized  $TiO_2$  are characteristic of the anatase phase, according to JCPDS #75-1537. The crystallite size ( $d$ ) was determined from  $TiO_2$  anatase diffractogram using the Debye-Scherrer Equation (4):

$$d = \frac{k\lambda}{\beta \cos \theta} \quad (4)$$

where  $\lambda$  is the wavelength of the X-ray (1.5406 Å),  $\beta$  is the full width at half-maximum (FWHM) of the diffraction peak,  $\theta$  is the diffraction angle, and  $k$  is a constant. A particle size of 21 nm was obtained using the peak at  $48^\circ$ . The inset of Figure 5 displays SEM images of the  $\text{TiO}_2$  nanoparticles, revealing a particle size of approximately 20 nm, which aligns with the value calculated from XRD [111,112].



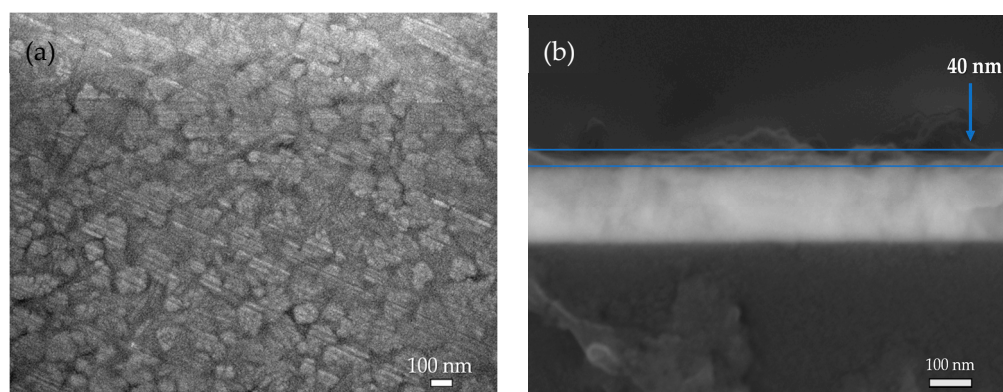
**Figure 4.** FT-IR spectra of different  $\text{TiO}_2$  nanomaterials: (a) commercial P25; (b) non-treated synthesized  $\text{TiO}_2$  ( $\text{TiO}_2$ ); (c) heat-treated synthesized  $\text{TiO}_2$  ( $\text{TiO}_2\text{-T}$ ); (d) UV-treated synthesized  $\text{TiO}_2$  ( $\text{TiO}_2\text{-V}$ ).



**Figure 5.** XRD diffraction pattern of synthesized  $\text{TiO}_2$  powder showing characteristic anatase peaks (to JCPDS #75-1537). Synthesized  $\text{TiO}_2$  presented an average particle size of 20 nm and approximately spherical morphology.

### 7.3. SEM Images of Deposited Films

To observe the TiO<sub>2</sub> film morphology, a JEOL JSM-7600F field emission scanning electron microscope was used. To estimate the nanoparticle size and film thickness, multiple micrographs of the sample surface and cross-section were captured at various locations. Several SEM images taken at different locations of the samples help to assess a careful estimation of the particle size and film thickness. Statistical analysis was performed to determine the average particle size or film thickness using captured micrographs and the ImageJ processing program. Figure 6a shows an SEM image of the compact layer from the top-down perspective, illustrating a homogeneous surface with the large grains of the underlying ITO substrate visible, suggesting the appropriate execution of the deposition technique. The cross-sectional image further illustrates that the film has a thickness of approximately 40 nm, in agreement with the desired value for a compact layer (Figure 6b). Figure 7 shows that the prepared nanostructured, mesoporous TiO<sub>2</sub> films processed with the low-temperature treatment are homogeneous. As can be observed, the particles are close together implying good interparticle bonding. The inset in Figure 7 shows a cross-section of the film, demonstrating a uniform film thickness of about 6.4 μm. This observation demonstrates that the film thickness approximates the optimal values typically observed for DSSCs. Additionally, it can be observed that the film is in direct contact with the blocking layer.



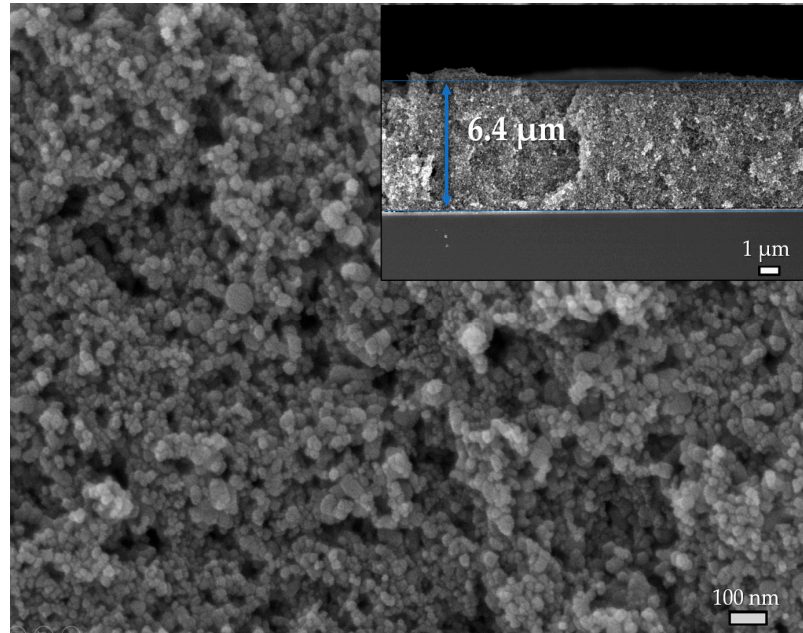
**Figure 6.** SEM images of the deposited low-temperature blocking: (a) plane view of the surface layer revealing homogeneous deposition and (b) cross-sectional image showing a layer thickness of about 40 nm.

Figure 8 shows SEM images of the counter electrode catalyzed with electropolymerized PEDOT. The formation of a granular structure resulting from the deposition process is observed, effectively increasing the surface roughness, thereby promoting enhanced electrocatalytic performance. The inset within Figure 8 provides visual evidence illustrating an average thickness of approximately 80 nm.

### 7.4. PV Characterization and J–V Curves of Rigid and F-DSSC

For measurements under 1 sun illumination, a 450 W ozone-free Xe lamp (Oriel) with a 10 cm water filter and an AM 1.5G optical filter was used. For low light intensity measurements at 1000 lux (5600 K), a Getlabs (Mexico) LED-based indoor lighting simulator was used. PV parameters and average  $\pm$  standard deviation (SD) of devices fabricated on ITO-coated glass using ACN:VN, VN:ACN, and MN electrolyte configurations are shown in Tables 2–4, respectively. Five devices, named 1 to 5, were fabricated for each configuration. Devices fabricated on ITO-coated glass using ACN:VN obtained the highest  $V_{OC}$  and FF, 0.76 V and 0.59, respectively (Device 2 in Table 2), whereas the highest  $J_{SC}$  was obtained for the VN:ACN with 6.94 mA cm<sup>-2</sup> (Device 3 in Table 2). The highest power conversion efficiency was obtained for VN:ACN devices with 2.62% (Device 3 in Table 2). Given that this configuration exhibited the highest efficiency, F-DSSCs were manufactured

employing this setup. PV parameters and average  $\pm$  SD of five F-DSSCs, named 1 to 5, fabricated on ITO-coated PEN with this optimum configuration are shown in Table 5. The best device for this set showed a  $J_{SC}$  of  $2.81 \text{ mA cm}^{-2}$ ,  $V_{OC}$  of 0.66 V, and FF of 0.52 with an efficiency of 1% (Device 2 in Table 5). Table 6 shows the comparison between average  $\pm$  SD values of all devices measured under 1 sun.



**Figure 7.** SEM images of the nanostructured, mesoporous  $\text{TiO}_2$  film demonstrating that the deposition was homogeneous with a thickness of about  $6.4 \mu\text{m}$ .

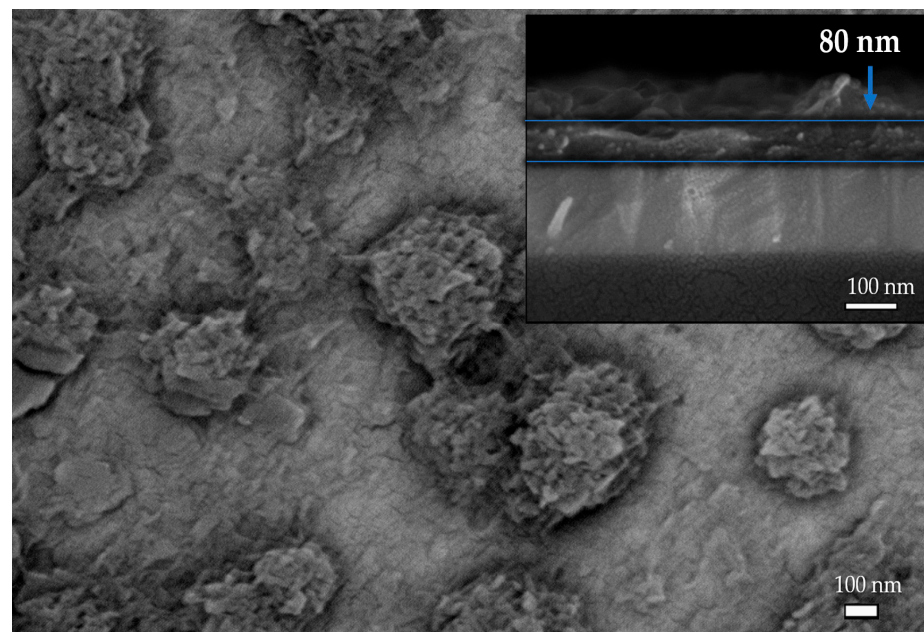


**Figure 8.** SEM images of the electrodeposited PEDOT counter electrode catalyst. An irregular surface with a granular structure can be observed. The average thickness is about 80 nm.

**Table 2.** Current density vs. voltage (J–V) data for DSSC devices fabricated on ITO-coated glass using ACN:VN (85:15 acetonitrile/valeronitrile) electrolyte configuration under 100 mW cm<sup>−2</sup>.

ACN:VN Device	V <sub>OC</sub> /V	J <sub>SC</sub> /mA cm <sup>−2</sup>	FF	η/%
1	0.76	4.30	0.59	1.94
2	0.76	4.36	0.59	1.97
3	0.69	2.92	0.54	1.10
4	0.76	4.23	0.59	1.92
5	0.70	3.45	0.58	1.71
Average ± SD	0.73 ± 0.02	3.85 ± 0.28	0.58 ± 0.02	1.73 ± 0.16

**Table 3.** Current density vs. voltage (J–V) data for DSSC devices fabricated on ITO-coated glass using VN:ACN (85:15 valeronitrile/acetonitrile) electrolyte configuration under 100 mW cm<sup>−2</sup>.

VN:ACN Device	V <sub>OC</sub> /V	J <sub>SC</sub> /mA cm <sup>−2</sup>	FF	η/%
1	0.69	6.82	0.54	2.05
2	0.73	6.89	0.51	2.59
3	0.71	6.94	0.51	2.62
4	0.73	6.82	0.51	2.58
5	0.72	6.92	0.51	2.61
Average ± SD	0.72 ± 0.01	6.60 ± 0.29	0.52 ± 0.01	2.49 ± 0.11

**Table 4.** Current density vs. voltage (J–V) data for DSSC devices fabricated on ITO-coated glass using MN (3-methoxypropionitrile) electrolyte configuration under 100 mW cm<sup>−2</sup>.

MN Devices	V <sub>OC</sub> /V	J <sub>SC</sub> /mA cm <sup>−2</sup>	FF	η/%
1	0.55	5.56	0.58	1.78
2	0.55	5.60	0.57	1.78
3	0.55	5.64	0.57	1.79
4	0.56	3.02	0.60	1.03
5	0.55	5.57	0.58	1.78
Average ± SD	0.55 ± 0.01	5.08 ± 0.51	0.58 ± 0.01	1.63 ± 0.15

**Table 5.** Current density vs. voltage (J–V) data for DSSC devices fabricated on ITO-coated PEN using ACN:VN (85:15 acetonitrile/valeronitrile) electrolyte configuration under 100 mW cm<sup>−2</sup>.

F-DSSC	V <sub>OC</sub> /V	J <sub>SC</sub> /mA cm <sup>−2</sup>	FF	η/%
1	0.65	3.13	0.37	0.77
2	0.66	2.81	0.52	1.00
3	0.67	2.45	0.59	0.98
4	0.66	2.42	0.60	0.97
5	0.67	2.47	0.59	0.99
Average ± SD	0.67 ± 0.01	2.73 ± 0.11	0.54 ± 0.43	0.97 ± 0.05

**Table 6.** Current density vs. voltage (J–V) average ± SD data for DSSC devices using three different electrolytes configurations under 100 mW cm<sup>−2</sup>. ACN:VN corresponds to devices using 85:15 acetonitrile/valeronitrile, VN:ACN to devices using 15:85 acetonitrile/valeronitrile, and MN to devices using 3-methoxypropionitrile. F-DSSC devices are fabricated using 15:85 acetonitrile/valeronitrile.

Device	V <sub>OC</sub> /V	J <sub>SC</sub> /mA cm <sup>−2</sup>	FF	η/%
ACN:VN <sup>a</sup>	0.73 ± 0.02	3.85 ± 0.28	0.58 ± 0.02	1.73 ± 0.16
VN:ACN <sup>a</sup>	0.72 ± 0.01	6.60 ± 0.29	0.52 ± 0.01	2.49 ± 0.11
MN <sup>a</sup>	0.55 ± 0.01	5.08 ± 0.51	0.58 ± 0.01	1.63 ± 0.15
F-DSSC <sup>b</sup>	0.67 ± 0.01	2.73 ± 0.11	0.54 ± 0.43	0.97 ± 0.05

<sup>a</sup> Rigid devices on ITO-coated glass. <sup>b</sup> Flexible devices on ITO-coated PEN.

Figure 9 shows the J–V curves of the best devices for each configuration of the DSSCs fabricated using low-temperature processing, i.e., Device 2 for ACN:VN, Device 3 for VN:ACN, Device 3 for MN, and Device 2 for F-DSSC. It can be concluded that the results on ITO/glass are generally better than observed for the ITO/PEN, even while using the exact same fabrication conditions, illustrating the complexity of the system.

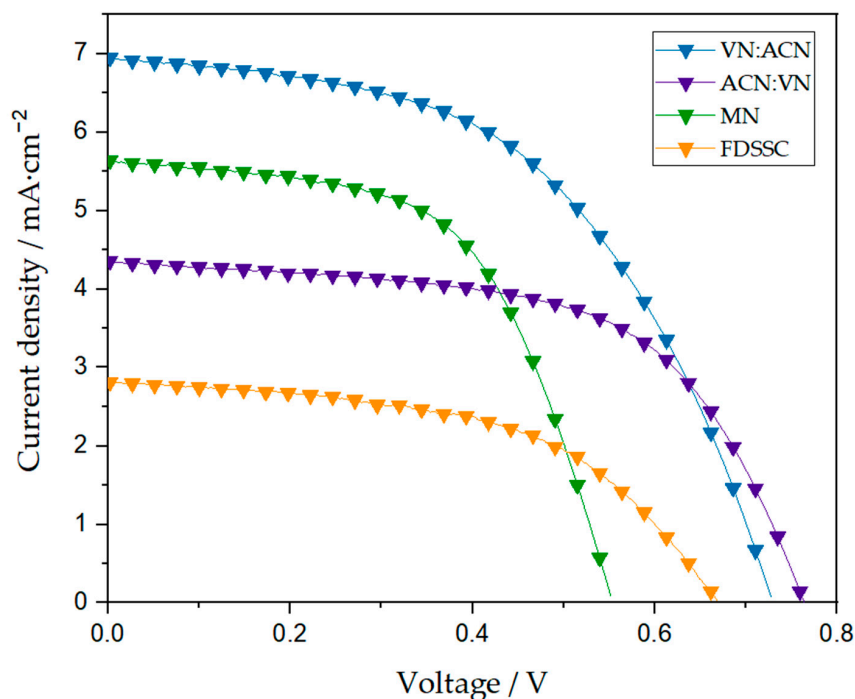


**Figure 9.** J–V curves of the best devices for each batch of the low-temperature DSSC-fabricated measured under 1 sun, i.e., Device 2 for ACN:VN, Device 3 for VN:ACN, Device 3 for MN, and Device 2 for F-DSSC.

PV parameters and the average  $\pm$  SD of devices measured under 1000 lux LED (5600 K) using the ACN:VN electrolyte configuration fabricated on ITO-coated glass and ITO-coated PEN are shown in Tables 7 and 8, respectively. Five devices were tested in each setup, named 1 to 5. Under low-light intensity, the best device fabricated on ITO-coated glass with the optimal configuration showed a  $V_{OC}$  of 0.55 V,  $J_{SC}$  of  $35.40 \mu\text{A cm}^{-2}$ , an FF of 0.44, and a maximum power output (MPO) of  $8.76 \mu\text{W cm}^{-2}$  (Device 5 in Table 7). The best device fabricated on ITO-coated PEN obtained a  $V_{OC}$  of 0.47,  $J_{SC}$  of  $17.11 \mu\text{A cm}^{-2}$ , FF of 0.47, and a maximum power output of  $4.26 \mu\text{W cm}^{-2}$  (Device 2 in Table 8). Table 9 shows the average  $\pm$  SD comparison of devices measured under low-light conditions.

**Table 7.** Current density vs. voltage (J–V) data for DSSC devices fabricated on ITO-coated glass using ACN:VN (85:15 acetonitrile/valeronitrile) electrolyte configuration under a 1000 lux LED (5600 K).

DSSC	$V_{OC}/\text{V}$	$J_{SC}/\mu\text{A cm}^{-2}$	FF	$\text{MPO}/\mu\text{W cm}^{-2}$
1	0.52	35.60	0.46	8.66
2	0.52	34.42	0.47	8.51
3	0.52	35.69	0.46	8.66
4	0.54	32.42	0.45	8.02
5	0.55	35.40	0.44	8.76
Average $\pm$ SD	$0.53 \pm 0.01$	$34.70 \pm 0.61$	$0.45 \pm 0.01$	$8.52 \pm 0.13$

Figure 10 shows the J–V curves under 1000 lux illumination of the best devices for the DSSCs fabricated using low-temperature processing on ITO/glass and ITO/PEN, i.e., Device 5 and Device 2, respectively. From Tables 7–9 and Figure 10, it can be seen that, similarly to results obtained under 1 sun illumination, the performance of DSSCs based on

ITO/glass is generally better than for ITO/PEN substrates depending on various factors. In general, higher optical transparency, less surface roughness, and better thermal and mechanical stability are the main reasons for the better performance of DSSCs based on ITO/glass compared to those on ITO/PET. Higher optical transparency allows a greater amount of light to reach the active layer of the DSSC, enhancing light absorption and hence cell efficiency. A smoother surface of ITO/glass substrates promotes better adhesion of subsequent layers, such as the compact and mesoporous titania layers and, hence, photoactive dye and electrolyte, resulting in improved charge transport and reduced charge recombination within the cell. In addition, ITO/glass substrates are more resistant to thermal expansion and contraction, minimizing the potential for cracks.

**Table 8.** Current density vs. voltage (J–V) data for DSSC devices fabricated on ITO-coated PEN using ACN:VN (85:15 acetonitrile/valeronitrile) electrolyte configuration under a 1000 lux LED (5600 K).

F-DSSC	$V_{OC}/V$	$J_{SC}/\mu A\ cm^{-2}$	FF	$MPO/\mu W\ cm^{-2}$
1	0.47	18.27	0.46	4.02
2	0.47	17.11	0.47	4.26
3	0.44	17.59	0.47	3.76
4	0.46	15.17	0.52	3.71
5	0.46	15.24	0.45	3.21
Average $\pm$ SD	$0.46 \pm 0.01$	$16.67 \pm 0.63$	$0.47 \pm 0.01$	$3.80 \pm 0.17$

**Table 9.** Current density voltage (J–V) average  $\pm$  SD data for rigid and F-DSSC devices using ACN:VN (85:15 acetonitrile/valeronitrile) measured under a 1000 lux LED, 5600 K.

Device	$V_{OC}/V$	$J_{SC}/\mu A\ cm^{-2}$	FF	$MPO/\mu W\ cm^{-2}$
ITO-coated Glass	$0.53 \pm 0.01$	$34.70 \pm 0.61$	$0.45 \pm 0.01$	$8.52 \pm 0.13$
ITO-coated PEN	$0.46 \pm 0.01$	$16.67 \pm 0.63$	$0.47 \pm 0.01$	$3.80 \pm 0.17$

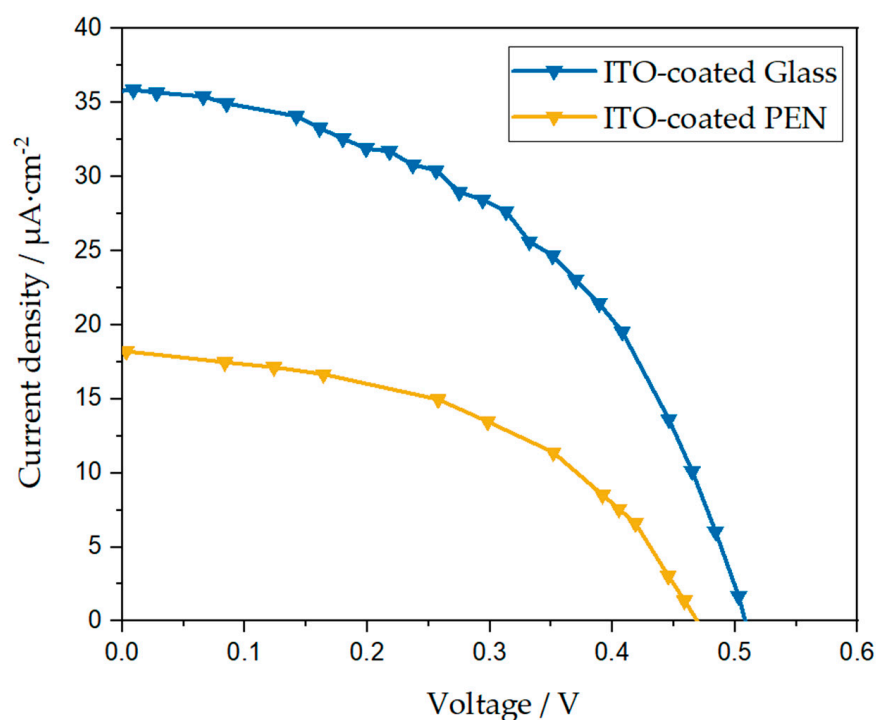


**Figure 10.** J–V curves of the best low-temperature DSSC fabricated measured under low-light intensity (1000 lux LED (5600 K) on both ITO-coated glass and PEN substrates using a mixture of 15:85 valeronitrile/acetonitrile as solvent, i.e., Device 5 and Device 2, respectively.

## 8. Discussion

TiO<sub>2</sub> nanoparticles were synthesized by sol–gel processing, and FTIR measurements revealed that the powders still contained some organic compounds after washing and air-drying. Hence, the cleaning process of the TiO<sub>2</sub> nanoparticle surface is a crucial step. The presence of organic compounds on the surface can affect the paste preparation by hindering bonding sites between TiO<sub>2</sub> nanoparticles and the ITO surface. In addition, a TiO<sub>2</sub> film with organic compounds can reduce the availability of active sites for the dye to anchor onto the surface, resulting in a lower dye loading. Impurities may also hinder the device performance, as they act as potential surface states that cause electron transport problems by increasing the charge transport resistance and, thus, electronic recombination since the electrons spend more time in contact with the redox electrolyte solution.

Low-temperature pastes without post-cleaning treatment showed poor adherence when deposited onto the blocking layer. In order to clean the TiO<sub>2</sub> nanomaterials, both heat treatment and UV treatment were employed, where the heat treatment was shown to produce a cleaner TiO<sub>2</sub> surface. It is important to point out that after the sol–gel synthesis process, it is necessary to remove the excess organic compounds with ethanol and dry the nanomaterial to powder before the 450 °C heat treatment; otherwise, some rutile is formed after heating. According to the FTIR spectra, powders processed with heat treatment presented fewer organic compounds. Although the thermal treatment rendered a cleaner surface in comparison with UV irradiation, it is crucial to develop methods that consume less energy. Therefore, exploring an optimized UV-radiation-based cleaning method holds promise, given its potential advantage for low cost and time saving.

A low-temperature aqueous paste without any organic binders was prepared by the addition of H<sub>2</sub>TiF<sub>6</sub> as an interparticle “binding” agent. The procedure for depositing the compact layer, as well as the preparation of the paste using H<sub>2</sub>TiF<sub>6</sub> as a binding agent between particles, has proven to be a technique that can be applied to industrial processes proposed in the literature for large-scale, continuous manufacturing. In both cases, the maximum temperature used was 120 °C. The paste deposition on the ITO substrate demonstrated sufficient adhesion. These findings demonstrate the high quality and integrity of the deposited film, supporting its suitability for future applications. For the fabrication of solar cells, a mechanically stable, homogeneous film with a thickness of about 6.4 μm was deposited on both rigid and FPCSs by doctor blading without any additional sintering treatment.

PEDOT was electrodeposited at room temperature using a water-based electrolyte, accomplishing the process within a brief duration of 60 s. The morphology achieved in the PEDOT electrodeposition, along with the attained thickness, aligns with the anticipated characteristics for this type of material. This conclusively demonstrates its potential for future applications and underscores its suitability for further investigation and exploration. In addition, this expeditious time frame renders it an easily reproducible method for large-scale manufacturing processes. A fast UV-curable resin was employed to seal the photo and counter electrode, avoiding high temperatures in the process.

Three different electrolytes were prepared by changing the solvents proportions (ACN:VN, VA:ACN, and MN). Rigid and flexible devices were tested under standard irradiation conditions (100 mW/cm<sup>2</sup>, AM 1.5). The variation of solvent composition in the electrolyte yielded different efficiencies demonstrated by the fabricated devices. From this point onwards, the next analysis will be conducted with reference to Table 6 since it summarizes the average and standard deviation of all configurations tested under 1 sun. Rigid devices fabricated with VN:ACN, ACN:VN, and MN obtained efficiencies of  $2.49 \pm 0.11\%$ ,  $1.73 \pm 0.16\%$ , and  $1.63 \pm 0.15\%$ , respectively, under 1 sun. The variations observed in the results can be attributed to the intrinsic properties of the employed solvents. The viscosity of the solvents exhibits an increase in the order of acetonitrile, followed by valeronitrile and, finally, 3-methoxypropionitrile. It is therefore expected that the viscosity of the electrolytes follows an increasing order of ACN:VN < VN:ACN < MN. It is evident that the current exhibits a complex relation to the viscosity, as J<sub>SC</sub> increases from  $3.85 \pm 0.28$  to

$6.6 \pm 0.29 \text{ mA cm}^{-2}$  in the acetonitrile/valeronitrile mixture in response to an increase in viscosity. Conversely, the viscosity of the 3-methoxy propionitrile is even higher, and in this case, the current undergoes a reduction to a value of  $5.08 \pm 0.51 \text{ mA cm}^{-2}$ .

The incorporation of various electrolyte formulations may affect the rate of electron injection to the  $\text{TiO}_2$  conduction band or dye regeneration by the redox shuttle species, while simultaneously imposing constrictions on the electronic transport phenomena within the  $\text{TiO}_2$  crystalline network [113]. The viscosity of the solvent directly impacts ion diffusion within the electrolyte, where a higher viscosity generally leads to a lower photocurrent due to mass transport limitations of the redox shuttle thus affecting the kinetics of dye regeneration [114–116]. In this instance, the utilization of the low-temperature N719-sensitized film demonstrates an impediment to achieving efficient electronic injection when employing the conventional ACN:VN solvent mixture at a ratio of 85:15, while better performance is observed for the VN:ACN system. The increase in the short-circuit photocurrent from  $3.85 \pm 0.28$  to  $6.60 \pm 0.29 \text{ mA cm}^{-2}$  may be ascribed to a decrease in the barrier for charge injection due to a slight positive shift of the conduction band edge of  $\text{TiO}_2$  [117] in relation to the increase in viscosity, i.e., different arrangement of species within the electrolyte, which can be inferred from the accompanying small decrease in  $V_{\text{OC}}$ .

In contrast, the higher electrolyte viscosity of the MN electrolyte solution slows down ionic diffusion sufficiently to affect the regeneration of dye molecules, which can be observed by the decrease in  $J_{\text{SC}}$ . Notwithstanding, the MN solvent exhibits a slightly larger photocurrent compared to the ACN:VN solvent system, which suggests that for this low-temperature system, an increased viscosity in the electrolyte may have a certain positive effect in the electron injection to the  $\text{TiO}_2$  conduction band by the dye. However, it is evident that there exists an optimal viscosity value. The  $V_{\text{OC}}$  shows a clear trend downward as the viscosity increases from  $0.73 \pm 0.01$ ,  $0.72 \pm 0.01$  to  $0.55 \pm 0.01 \text{ V}$  for ACN:VN, VN:CAN, and MN, respectively. It is well known that the ACN:VN electrolyte configuration can reduce recombination, thus improving the  $V_{\text{OC}}$  and FF of a device [118]. A slight decrease of approximately 10 mV in  $V_{\text{OC}}$  is observed when comparing ACN:VN with VN:ACN devices. This indicates that the increase in viscosity could also exert a subtle promoting effect on electronic recombination in VN:ACN devices since a higher electron density in the conduction band is expected for the increased  $J_{\text{SC}}$ . In the case of MN devices, a more pronounced decrease in  $V_{\text{OC}}$  is observed. In this regard, a substantial difference compared with ACN:VN, and VN:CAN configurations is that MN electrolyte does not use additives in its formulation. The main reason for using MN electrolyte is its compatibility with low-temperature configurations, as demonstrated previously, and the good results obtained with its continual utilization [55,119].

Additives play a pivotal role in the optimization of PV performance. They exert a pronounced influence on increasing the  $V_{\text{OC}}$  by attenuating recombination kinetics while concurrently inducing shifts in the energy of the band edges [117,120,121]. In the case of MN devices, this effect can be readily observed by a marked drop of 180 mV compared with ACN:VN devices. The FF within a DSSC can be influenced by carrier diffusion within the electrolyte, related to a series resistance [16]. It can be observed that the ACN:VN devices achieved the best FF value of  $0.58 \pm 0.02$ . In this system, electron injection from the dye to the  $\text{TiO}_2$  conduction band is apparently hampered. This may result in a longer time for the oxidized species in the electrolyte to regenerate fewer dye molecules, thus avoiding charge transport issues compared with VN:ACN and MN configurations. In the case of VN:ACN, the FF is notably lower with a value of  $0.52 \pm 0.01$ . This could be due to a combined effect of improved electronic injection and a more viscous solvent. Ionic diffusion may be more affected due to a more pronounced difference in ion concentration resulting from higher current flow [122], hence rendering more noticeable ion transport issues. Remarkably, MN demonstrated an FF close to that demonstrated by ACN:VN, with a value of  $0.58 \pm 0.01$ . The rate of ionic diffusion appears to be more beneficial in this system as viscosity increases. The slower electron injection rate observed in this system compared to VN:ACN and a slower diffusion could potentially positively impact FF by promoting a well-balanced ion

concentration and facilitating optimal charge-carrier diffusion within the electrolyte. Note that the FF is also affected by the recombination mechanism and kinetics, which may also differ significantly for the different solvents. As evident from the FTIR graph, organic compounds are still observable on the surface of TiO<sub>2</sub>, even after post-heat treatments. These compounds may act as surface states, impeding efficient electronic transport within the nanomaterial [105]. This factor could have a negative influence by imposing constraints on the photocurrent exhibited in the devices, consequently impeding a better performance.

A DSSC with the optimum electrolyte configuration was fabricated on an ITO-coated PEN substrate. The F-DSSC yielded an efficiency of 1.0% under 1 sun. F-DSSCs showed a  $V_{OC}$  of  $0.67 \pm 0.01$  V, which suggests the presence of a certain degree of recombination in this system. However, the  $V_{OC}$  of F-DSSC devices was higher than the rigid MN devices, providing further evidence for the enhanced compatibility of the VN:ACN composition with the low-temperature system. F-DSSC devices exhibited a  $J_{SC}$  of  $2.73 \pm 0.11$  mA cm<sup>-2</sup>, which is comparatively lower than all other systems. On the other hand, the FF of  $0.54 \pm 0.43$  remained close to the expected value for this system, as demonstrated by VN:ACN devices.

Finally, rigid and flexible VN:ACN devices were tested under an indoor light simulator at 1000 lux. The next analysis will be conducted with reference to Table 9 since it summarizes the average and standard deviation of rigid and F-DSSCs tested under simulated low-light conditions. It can be observed that the  $V_{OC}$  of both devices are significantly different,  $0.53 \pm 0.01$  V for ITO-coated glass devices and  $0.46 \pm 0.01$  V for ITO-coated PEN devices, whereas FF maintained approximately the same value of  $0.45 \pm 0.01$  and  $0.47 \pm 0.01$ , respectively. A more significant disparity is evident in  $J_{SC}$ . Devices fabricated on glass substrates exhibited almost double the photocurrent compared to those on FPCSs, measuring  $16.67 \pm 0.63$  and  $34.70 \pm 0.61$   $\mu$ A cm<sup>-2</sup>, respectively. Maximum power outcomes of  $8.52 \pm 0.13$  and  $3.80 \pm 0.17$   $\mu$ W cm<sup>-2</sup> were obtained for rigid and flexible devices, respectively. Hence, in both high-intensity and low-intensity measurements, the F-DSSCs exhibited lower performance compared to rigid devices.

Under low-light conditions, the photoinduced electron transfer exhibits a notable reduction in comparison to high-intensity illumination in solar cells, attributable to the low photon flux [117]. The dependency of solar cell output power on the spectral composition of the incoming light is a widely recognized phenomenon [123,124]. At low light intensities, minimizing recombination processes becomes a major task. It is crucial to optimize the compact layer to prevent unwanted interaction between the TCO/electrolyte interface while simultaneously facilitating effective electrical contact between the TiO<sub>2</sub> film and the TCO [32].

Two key factors account for the lower photoelectric performance observed in low-temperature methods. Firstly, it can be attributed to the inadequate interparticle connection of TiO<sub>2</sub> impeding efficient electron transport [59], consequently limiting the overall device performance. In this regard, although the films deposited from the low-temperature paste demonstrated sufficient mechanical stability, further research is needed to explore the incorporation of suitable low-temperature methods to enhance this aspect while remaining compatible with large-scale production processes. Secondly, an unsatisfactory electrical connection between TiO<sub>2</sub> and ITO is evident, leading to an increase in series resistance. This additional resistance impedes the captured electrons from generating optimal electrical work, directly impacting the efficiency and performance of the solar cells [77].

In this work, we attribute this behavior to the quality of the ITO on the surface of the FPCS, as well as any potential drawbacks that may arise during the fabrication process of these devices, such as possible electrolyte leaks. It was demonstrated that washing the substrates following the utilized protocol increased the surface energy of the substrate, rendering it more hydrophilic. This effect facilitated the proper spreading of the water-based paste upon deposition, leading to improved adherence to the substrate. However, owing to the fragile nature of the ITO layer on the PEN substrate as well as the acidity of the paste (pH = 2) this could have resulted in damaging the layer and losing electronic contact sites between TiO<sub>2</sub> and ITO and, thus, yielding a lower efficiency compared to rigid devices.

Significantly, the distinction in performance between rigid and flexible devices becomes less pronounced for low-intensity regimes, which is an interesting observation warranting future research into the use of this low-temperature configuration for indoor applications. Hence, it is necessary to conduct a careful study to find an optimal balance between the pre-treatment of the ITO surface and the acidity of the paste used for improved performance.

Another consideration for the improvement of the low-temperature paste is to optimize the concentration of dispersed TiO<sub>2</sub> nanoparticles in the solvents to achieve a smaller film thickness. Future work aimed at reducing the film thickness to enhance the electronic diffusion distance over film thickness ratio is in progress. In this regard, the approach of film compression holds substantial promise based on extensive evidence that this method significantly improves the quality of the deposited film. Another avenue for advancement involves the utilization of an organic dye with a high molar extinction coefficient, which holds promise for enhancing the performance and efficiency of the ultra-thin-film systems. In addition, organic dyes are characterized by having bulky ligands that modify the chemical environment of the redox couple in the vicinity of the TiO<sub>2</sub> surface, which may minimize recombination [118].

## 9. Conclusions

Seminal studies have established solid foundations and generated cutting-edge knowledge in the field of F-DSSCs. These pioneering investigations have paved the way for more advanced approaches and laid the groundwork for current developments in the field contributing to its advancement and ongoing development. The demonstrated efficacy of these approaches paves the way for advances in the development of cost-effective and environmentally friendly solar energy technologies. Further research and optimization efforts will undoubtedly contribute to the realization of highly efficient and commercially viable flexible solar cells. In this regard, the results obtained in this study demonstrate the feasibility of the low-temperature, rapid, and simple fabrication process for flexible solar cells.

Different low-temperature approaches were carried out in order to fabricate an F-DSSC for indoor applications by simple and reproducible methods without the addition of complex steps in the fabrication process. Three different electrolytes were prepared by changing the solvents used in the formulations named ACN:VN, VN:CAN, and MN. Rigid and flexible devices were fabricated using fast and simple low-temperature processes which are compatible with scale-up. Devices were measured under simulated high and low light intensities. Rigid VN:ACN devices showed the best efficiency of 2.62% under 1 sun. Flexible devices using VN:ACN electrolyte configuration achieved an efficiency of 1.00% under 1 sun. Under low-light illumination, these rigid and flexible devices demonstrated a maximum power output of  $8.52 \pm 0.13$  and  $3.80 \pm 0.17 \mu\text{W cm}^{-2}$ , respectively.

We have found that VN:ACN is a novel electrolyte configuration that shows excellent compatibility with our low-temperature TiO<sub>2</sub> paste. Despite the low efficiency of the F-DSSC compared to the glass-based device with the same configuration, this electrolyte solution proved to be superior to the MN. We believe that the notable coupling can be ascribed to the existence of an optimal viscosity range, which promotes favorable electronic injection mechanisms, efficient electronic collection, and precise positioning of the Fermi level. These findings highlight the potential for scalable production and commercialization of flexible solar devices. The approach presented has the potential to ensure efficient F-DSSCs without compromising the simplicity of the fabrication process and contribute significantly to the progress of research in this area.

**Author Contributions:** Conceptualization, investigation, methodology, data analysis, writing—original draft preparation, R.A.-B.; conceptualization, supervision, project administration, investigation, writing—review and editing, G.O.; conceptualization, supervision, investigation, methodology, writing—review and editing, D.P. All authors have read and agreed to the published version of the manuscript.

**Funding:** This research was funded by CONACYT (Mexico) under the FORDECYT-PRONACES projects 318703 and 848260 and the Basic Sciences grant CB-A1-S-21018. The authors also acknowledge funding from the Ministerio de Ciencia e Innovación of Spain, Agencia Estatal de Investigación (AEI), and the European Regional Development Fund (FEDER) under Grant PID2019-110430GB-C22 and the Royal Society (UK) International Collaboration Award, ICA\R1\191321. G.O. gratefully acknowledges support from the Ministerio de Universidades and Universidad Pablo de Olavide (Spain) through the Beatriz Galindo program under Project BEAGAL 18/00077 and Grant BGP 18/00060.

**Data Availability Statement:** All data will be available upon request.

**Acknowledgments:** We would like to acknowledge Beatriz Heredia Cervera, Jose Bante Guerra, Daniel Aguilar, and Victor Rejón for technical assistance, the “Laboratorio Nacional de Nano y Biomateriales” (LANNBIO), CINVESTAV, Mérida, for support, and also Jose Bante Guerra for the fabrication of the indoor solar simulator.

**Conflicts of Interest:** The authors declare no conflict of interest.

## References

1. Kim, M.B.; Han, H.G.; Roh, D.H.; Park, J.; Kim, K.M.; Kim, U.Y.; Kwon, T.H. Flexible Dye-Sensitized Solar Cells. In *Flexible Energy Conversion and Storage Devices*, 1st ed.; Zhi, C., Dai, L., Eds.; Wiley-VCH Verlag GmbH & Co.: Weinheim, Germany, 2018; pp. 239–281.
2. Mozaffari, S.; Nateghi, M.R.; Zarandi, M.B. An overview of the Challenges in the commercialization of dye sensitized solar 1362 cells. *Renew. Sustain. Energy Rev.* **2017**, *71*, 675–686. [CrossRef]
3. Baby, R.; Nixon, P.D.; Kumar, N.M.; Subathra, M.S.P.; Ananthi, N. A comprehensive review of dye-sensitized solar cell 1368 optimal fabrication conditions, natural dye selection, and application-based future perspectives. *Environ. Sci. Pollut. Res.* **2022**, *29*, 371–404. [CrossRef]
4. Gong, J.; Sumathy, K.; Qiao, Q.; Zhou, Z. Review on dye-sensitized solar cells (DSSCs): Advanced techniques and research 1371 trends. *Renew. Sustain. Energy Rev.* **2017**, *68*, 234–246. [CrossRef]
5. Li, G.; Sheng, L.; Li, T.; Hu, J.; Li, P.; Wang, K. Engineering flexible dye-sensitized solar cells for portable electronics. *Solar Energy* **2018**, *177*, 80–98. [CrossRef]
6. Hashmi, G.; Miettunen, K.; Peltola, T.; Halme, J.; Asghar, I.; Aitola, K.; Toivola, M.; Lund, P. Review of materials and manufacturing options for large area flexible dye solar cells. *Renew. Sustain. Energy Rev.* **2011**, *15*, 3717–3732. [CrossRef]
7. Li, B.; Huang, F.; Zhong, J.; Xie, J.; Wen, M.; Pen, Y. Fabrication of Flexible Dye-Sensitized Solar Cell Modules using Commercially Available Materials. *Energy Technol.* **2016**, *4*, 536–542. [CrossRef]
8. Freitag, M.; Teuscher, J.; Saygili, Y.; Zhang, X.; Giordano, F.; Liska, P.; Hua, J.; Zakeeruddin, M.; Moser, J.E.; Grätzel, M.; et al. Dye-sensitized solar cells for efficient power generation under ambient lighting. *Nat. Photon.* **2017**, *11*, 372–378. [CrossRef]
9. Karthick, S.N.; Hemalatha, K.V.; Balasingam, S.K.; Clinton, F.M.; Akshaya, S.; Kim, H. Dye-Sensitized Solar Cells: History, Components, Configuration, and Working Principle. In *Interfacial Engineering in Functional Materials for Dye-Sensitized Solar*, 1st ed.; Pandikumar, A., Jothivenkatachalam, K., Bhojonaa, K.B., Eds.; Jhon Wiley & Sons: New York, NY, USA, 2020; pp. 1–16. [CrossRef]
10. Conibeer, G. Third-generation photovoltaics. *Mater. Today* **2007**, *10*, 11. [CrossRef]
11. Yan, J.; Saunders, B.R. Third-generation solar cells: A review and comparison of polymer:fullerene, hybrid polymer and perovskite solar cells. *RSC Adv.* **2014**, *4*, 43286. [CrossRef]
12. Mingsukang, M.A.; Buraidah, M.H.; Arof, A.K. Third-Generation-Sensitized Solar Cells. In *Nanostructured Solar Cells*, 1st ed.; Das, N., Ed.; InTechOpen: London, UK, 2017; pp. 7–31. [CrossRef]
13. Mahalingam, S.; Abdullah, H. Electron transport study of indium oxide as photoanode in DSSCs: A review. *Renew. Sustain. Energy Rev.* **2016**, *63*, 245–255. [CrossRef]
14. Buitrago, E.; Novello, A.M.; Meyer, T. Third-Generation Solar Cells: Toxicity and Risk of Exposure. *Helv. Chim. Acta* **2020**, *103*, 9. [CrossRef]
15. George, J.; Joseph, A.P.; Balachandran, M. Perovskites: Emergence of highly efficient third-generation solar cells. *Int. J. Energy Res.* **2022**, *46*, 21856–21883. [CrossRef]
16. Wu, J.; Lan, Z.; Lian, J.; Huang, M.; Huang, Y.; Fan, L.; Luo, G. Electrolytes in dye-sensitized solar cells. *Chem. Rev.* **2015**, *115*, 2136–2173. [CrossRef]
17. National Renewable Energy Laboratory. Available online: <https://www.nrel.gov/pv/cell-efficiency.html> (accessed on 26 June 2023).
18. Toivola, M.; Halme, J.; Miettunen, K.; Aitola, K.; Lund, P.D. Nanostructured dye solar cells on flexible substrates-Review. *Int. J. Energy Res.* **2009**, *33*, 1145–1160. [CrossRef]
19. Yugis, A.R.; Mansa, R.F.; Sipaut, C.S. Review on metallic and plastic flexible dye sensitized solar cell. *IOP Conf. Ser. Mater. Sci. Eng.* **2015**, *78*, 012003. [CrossRef]

20. Nogueira, A.F.; Longo, C.; De Paoli, M.A. Polymers in dye sensitized solar cells: Overview and perspectives. *Coord. Chem. Rev.* **2004**, *248*, 1455–1468. [[CrossRef](#)]
21. Miettunen, K.; Halme, J.; Lund, P. Metallic and plastic dye solar cells. *WIREs Energy Environ.* **2013**, *2*, 104–120. [[CrossRef](#)]
22. Miettunen, K.; Vapaavuori, J.; Poskela, A.; Tiihonen, A.; Lund, P.D. Recent progress in flexible dye solar cells. *WIREs Energy Environ.* **2018**, *7*, e302. [[CrossRef](#)]
23. Mariotti, N.; Bonomo, M.; Fagiolari, L.; Barbero, N.; Gerbaldi, C.; Bella, F.; Barolo, C. Recent advances in eco-friendly and cost-effective materials towards sustainable dye-sensitized solar cells. *Green Chem.* **2020**, *22*, 7168–7218. [[CrossRef](#)]
24. James, S.; Contractor, R. Study on Nature-inspired Fractal Design-based Flexible Counter Electrodes for Dye-Sensitized Solar Cells Fabricated using Additive Manufacturing. *Sci. Rep.* **2018**, *8*, 17032. [[CrossRef](#)]
25. Lin, L.Y.; Ho, K.C. Dye-sensitized solar cells. In *Encyclopedia of Modern Optics*, 2nd ed.; Guenther, B.D., Steel, D.G., Eds.; Elsevier Inc.: Amsterdam, The Netherlands, 2018; Volume 5, pp. 270–281. [[CrossRef](#)]
26. Ito, S. Investigation of Dyes for Dye-Sensitized: Ruthenium-Complex Dyes, Metal-Free Dyes, Metal-Complex Porphyrin Dyes. In *Solar Cells—Dye-Sensitized Devices*, 1st ed.; Kosyachenko, L.A., Ed.; InTechOpen: London, UK, 2011; pp. 19–48. [[CrossRef](#)]
27. Bella, F.; Bongiovanni, R. Photoinduced polymerization: An innovative, powerful and environmentally friendly technique for the preparation of polymer electrolytes for dye-sensitized solar cells. *J. Photochem. Photobiol. C.* **2013**, *16*, 1–21. [[CrossRef](#)]
28. Ellis, H.; Vlachopoulos, N.; Häggman, L.; Perruchot, C.; Jouini, M.; Boschloo, G.; Hagfeldt, A. PEDOT counter electrodes for dye-sensitized solar cells prepared by aqueous micellar electrodeposition. *Electrochim. Acta* **2013**, *107*, 45–51. [[CrossRef](#)]
29. Hagfeldt, A.; Boschloo, G.; Lindström, H.; Figgemeier, E.; Holmberg, A.; Aranyos, V.; Magnusson, E.; Malmqvist, L. A system approach to molecular solar cells. *Coord. Chem. Rev.* **2004**, *248*, 1501–1509. [[CrossRef](#)]
30. Park, N.G.; Kim, K.M.; Kang, M.G.; Ryu, K.S.; Chang, S.H.; Shin, Y.J. Chemical Sintering of Nanoparticles: A Methodology for Low-Temperature Fabrication of Dye-Sensitized TiO<sub>2</sub> Films. *Adv. Mater.* **2005**, *17*, 2349–2353. [[CrossRef](#)]
31. Lindström, H.; Holmberg, A.; Magnusson, E.; Lindquist, S.E.; Malmqvist, L.; Hagfeldt, A. A New Method for Manufacturing Nanostructured Electrodes on Plastic Substrates. *Nano Lett.* **2001**, *1*, 97–100. [[CrossRef](#)]
32. Michaels, H.; Rinderle, M.; Freitag, R.; Benesperi, I.; Edvinsson, T.; Socher, R.; Gagliardi, A.; Freitag, M. Dye-sensitized solar cells under ambient light powering machine learning: Towards autonomous smart sensors for the internet of things. *Chem. Sci.* **2020**, *11*, 2895–2906. [[CrossRef](#)]
33. Li, M.; Igbari, F.; Wang, Z.K.; Liao, L.S. Indoor Thin-Film Photovoltaics: Progress and Challenges. *Adv. Energy Mater.* **2020**, *10*, 2000641. [[CrossRef](#)]
34. Kim, S.; Jahandar, M.; Jeong, J.H.; Lim, D.C. Recent Progress in Solar Cell Technology for Low-Light Indoor Applications. *Curr. Altern. Energy* **2019**, *3*, 3–17. [[CrossRef](#)]
35. Zhang, D.; Stojanovic, M.; Ren, Y.; Cao, Y.; Eickemeyer, F.T.; Socie, E.; Vlachopoulos, N.; Moser, J.-E.; Zakeeruddin, S.M.; Hagfeldt, A.; et al. A molecular photosensitizer achieves a VOC of 1.24 V enabling highly efficient and stable dye-sensitized solar cells with copper(II/I)-based electrolyte. *Nat. Commun.* **2021**, *12*, 1777. [[CrossRef](#)]
36. Cao, Y.; Liu, Y.; Zakeeruddin, S.M.; Hagfeldt, A.; Grätzel, M. Direct Contact of Selective Charge Extraction Layers Enables High-Efficiency Molecular Photovoltaics. *Joule* **2018**, *2*, 1108–1117. [[CrossRef](#)]
37. Miettunen, K.; Halme, J.; Lund, P. Segmented cell design for improved factoring of aging effects in dye solar cells. *J. Phys. Chem. C* **2009**, *113*, 10297–10302. [[CrossRef](#)]
38. Ma, T.; Fang, X.; Akiyama, M.; Inoue, K.; Noma, H.; Abe, E. Properties of several types of novel counter electrodes for dye-sensitized solar cells. *J. Electroanal. Chem.* **2004**, *574*, 77–83. [[CrossRef](#)]
39. Karim, N.A.; Mehmood, U.; Zahid, H.F.; Asif, T. Nanostructured photoanode and counter electrode materials for efficient Dye-Sensitized Solar Cells (DSSCs). *Sol. Energy* **2019**, *185*, 165–188. [[CrossRef](#)]
40. Sen, A.; Putra, M.H.; Biswas, A.K.; Behera, A.K.; Groß, A. Insight on the choice of sensitizers/dyes for dye sensitized solar cells: A review. *Dyes Pigm.* **2023**, *213*, 111087. [[CrossRef](#)]
41. Wu, T.-C.; Huang, W.-M.; Meen, T.-H.; Tsai, J.-K. Performance Improvement of Dye-Sensitized Solar Cells with Pressed TiO<sub>2</sub> Nanoparticles Layer. *Coatings* **2023**, *13*, 907. [[CrossRef](#)]
42. Senthilarasu, S.; Peiris, T.A.N.; García-Cañadas, J.; Wijayantha, K.G.U. Preparation of nanocrystalline TiO<sub>2</sub> electrodes for flexible dye-sensitized solar cells: Influence of mechanical compression. *J. Phys. Chem. C* **2012**, *116*, 19053–19061. [[CrossRef](#)]
43. Upadhyaya, H.M.; Senthilarasu, S.; Hsu, M.H.; Kumar, D.K. Recent progress and the status of dye-sensitized solar cell (DSSC) technology with state-of-the-art conversion efficiencies. *Sol. Energy Mater. Sol. Cells* **2013**, *119*, 291–295. [[CrossRef](#)]
44. Wante, H.P.; Bala, S.; Romanus, I.O. Review: Low Temperature Sintering of TiO<sub>2</sub> for Dye Sensitized Solar Cells (DSSCs) Fabrication on Flexible Substrates. *Eur. J. Mater. Sci.* **2022**, *9*, 18–24. [[CrossRef](#)]
45. Inukai, K.; Takahashi, Y.; Ri, K.; Shin, W. Rheological analysis of ceramic pastes with ethyl cellulose for screen-printing. *Ceram Int.* **2015**, *41*, 5959–5966. [[CrossRef](#)]
46. Kunzmann, A.; Valero, S.; Sepúlveda, Á.E.; Rico-Santacruz, M.; Lalinde, E.; Berenguer, J.R.; García-Martínez, J.; Guldi, D.M.; Serrano, E.; Costa, R.D. Hybrid Dye-Titania Nanoparticles for Superior Low-Temperature Dye-Sensitized Solar Cells. *Adv. Energy Mater.* **2018**, *8*, 1702583. [[CrossRef](#)]
47. Kijitori, Y.; Ikegami, M.; Miyasaka, T. Highly efficient plastic dye-sensitized photoelectrodes prepared by low-temperature binder-free coating of mesoscopic titania pastes. *Chem. Lett.* **2007**, *36*, 190–191. [[CrossRef](#)]

48. Weerasinghe, H.C.; Sirimanne, P.M.; Simon, G.P.; Cheng, Y.-B. Cold isostatic pressing technique for producing highly efficient flexible dye-sensitized solar cells on plastic substrates. *Prog. Photovolt.* **2012**, *20*, 321–332. [[CrossRef](#)]
49. Morita, S.; Ikegami, M.; Wei, T.C.; Miyasaka, T. Quantum conversion enhancement with TiO<sub>x</sub> compact layers for ITO-plastic-film-based low-temperature-processed dye-sensitized photoelectrodes. *Chem. Phys. Chem.* **2014**, *15*, 1190–1193. [[CrossRef](#)] [[PubMed](#)]
50. Zhang, D.; Yoshida, T.; Minoura, H. Low Temperature Synthesis of Porous Nanocrystalline TiO<sub>2</sub> Thick Film for Dye-Sensitized Solar Cells by Hydrothermal Crystallization. *Chem. Lett.* **2002**, *31*, 874–875. [[CrossRef](#)]
51. Zhang, D.; Yoshida, T.; Furuta, K.; Minoura, H. Hydrothermal preparation of porous nano-crystalline TiO<sub>2</sub> electrodes for flexible solar cells. *J. Photochem. Photobiol. A Chem.* **2004**, *164*, 159–166. [[CrossRef](#)]
52. Stathatos, E.; Chen, Y.; Dionysiou, D.D. Quasi-solid-state dye-sensitized solar cells employing nanocrystalline TiO<sub>2</sub> films made at low temperature. *Sol. Energy Mater. Sol. Cells* **2008**, *92*, 1358–1365. [[CrossRef](#)]
53. Weerasinghe, H.C.; Sirimanne, P.M.; Franks, G.V.; Simon, G.P.; Cheng, Y.B. Low temperature chemically sintered nano-crystalline TiO<sub>2</sub> electrodes for flexible dye-sensitized solar cells. *J. Photochem. Photobiol. A Chem.* **2010**, *213*, 30–36. [[CrossRef](#)]
54. Weerasinghe, H.C.; Franks, G.V.; Plessis, J.D.; Simon, G.P.; Cheng, Y.B. Anomalous rheological behavior in chemically modified TiO<sub>2</sub> colloidal pastes prepared for flexible dye-sensitized solar cells. *J. Mater. Chem.* **2010**, *20*, 9954–9961. [[CrossRef](#)]
55. Holliman, P.J.; Connell, A.; Davies, M.; Carnie, M.; Bryant, D.; Jones, E.W. Low temperature sintering of aqueous TiO<sub>2</sub> colloids for flexible, co-sensitized dye-sensitized solar cells. *Mater. Lett.* **2019**, *236*, 289–291. [[CrossRef](#)]
56. Sasi, S.; Chandran, A.; Sugunan, S.K.; Krishna, A.C.; Nair, P.R.; Peter, A.; Shaji, A.N.; Subramanian, K.R.V.; Pai, N.; Mathew, S. Flexible Nano-TiO<sub>2</sub> Sheets Exhibiting Excellent Photocatalytic and Photovoltaic Properties by Controlled Silane Functionalization—Exploring the New Prospects of Wastewater Treatment and Flexible DSSCs. *ACS Omega* **2022**, *7*, 25094–25109. [[CrossRef](#)]
57. Miyasaka, T.; Ikegami, M.; Kijitori, Y. Photovoltaic Performance of Plastic Dye-Sensitized Electrodes Prepared by Low-Temperature Binder-Free Coating of Mesoscopic Titania. *J. Electrochem. Soc.* **2007**, *154*, A455. [[CrossRef](#)]
58. Li, X.; Lin, H.; Li, J.; Wang, N.; Lin, C.; Zhang, L. Chemical sintering of graded TiO<sub>2</sub> film at low-temperature for flexible dye-sensitized solar cells. *J. Photochem. Photobiol. A Chem.* **2008**, *195*, 247–253. [[CrossRef](#)]
59. Zhang, D.; Downing, J.A.; Knorr, F.J.; McHale, J.L. Room-temperature preparation of nanocrystalline TiO<sub>2</sub> films and the influence of surface properties on dye-sensitized solar energy conversion. *J. Phys. Chem. B.* **2006**, *110*, 21890–21898. [[CrossRef](#)] [[PubMed](#)]
60. Weerasinghe, H.C.; Sirimanne, P.M.; Simon, G.P.; Cheng, Y.B. Fabrication of efficient solar cells on plastic substrates using binder-free ball milled titania slurries. *J. Photochem. Photobiol. A Chem.* **2009**, *206*, 64–70. [[CrossRef](#)]
61. Dürr, M.; Schmid, A.; Obermaier, M.; Rosselli, S.; Yasuda, A.; Nelles, G. Low-temperature fabrication of dye-sensitized solar cells by transfer of composite porous layers. *Nat. Mater.* **2005**, *4*, 607–611. [[CrossRef](#)]
62. Kim, H.; Piqué, A.; Kushto, G.P.; Auyeung, R.C.Y.; Lee, S.H.; Arnold, C.B.; Kafafi, Z.H. Dye-sensitized solar cells using laser processing techniques. In *Photon Processing in Microelectronics and Photonics*, 3rd ed.; Dubowski, J.J., Geohegan, D.B., Träger, F., Herman, P.R., Fieret, J., Pique, A., Okada, T., Bachmann, F.G., Hoving, W., Washio, K., et al., Eds.; Proceedings of SPIE; The International Society for Optical Engineering: Bellingham, WA, USA, 2004; Volume 5339, p. 5339A-48. [[CrossRef](#)]
63. Kim, H.; Auyeung, R.C.Y.; Ollinger, M.; Kushto, G.P.; Kafafi, Z.H.; Piqué, A. Laser-sintered mesoporous TiO<sub>2</sub> electrodes for dye-sensitized solar cells. *Appl. Phys A* **2006**, *83*, 73–76. [[CrossRef](#)]
64. Shen, J.; Cheng, R.; Chen, Y.; Chen, X.; Sun, Z.; Huang, S. A Novel TiO<sub>2</sub> Tape for Fabricating Dye-Sensitized Solar Cells on Universal Conductive Substrates. *ACS Appl. Mater. Interfaces* **2013**, *5*, 13000–13005. [[CrossRef](#)]
65. Yang, L.; Wu, L.; Wu, M.; Xin, G.; Lin, H.; Ma, T. High-efficiency flexible dye-sensitized solar cells fabricated by a novel friction-transfer technique. *Electrochem Commun.* **2010**, *12*, 1000–1003. [[CrossRef](#)]
66. Lindström, H.; Södergren, S.; Lindquist, S.; Hagfeldt, A. Method for Manufacturing Nanostructured Thin Film Electrodes. World Intellectual Property Organization Patent Application No. WO 00/72373 A1, 20 November 2000.
67. Lindström, H.; Holmberg, A.; Magnusson, E.; Malmqvist, L.; Hagfeldt, A. A new method to make dye-sensitized nano-crystalline solar cells at room temperature. *J. Photochem. Photobiol. A Chem.* **2001**, *145*, 107–112. [[CrossRef](#)]
68. Lindström, H.; Magnusson, E.; Holmberg, A.; Södergren, S.-E.; Lindquist, S.-E.; Hagfeldt, A. A new method for manufacturing nanostructured electrodes on glass substrates. *Sol. Energy Mater. Sol. Cells* **2002**, *73*, 91–101. [[CrossRef](#)]
69. Lindström, H.; Boschloo, G.; Lindquist, S.-E.; Hagfeldt, A. A New Method for Manufacturing Dye-Sensitized Solar Cells on Plastic Substrates. In *Molecules as Components of Electronic Devices—ASC Symposium Series 844*; Marya, L., Ed.; American Chemical Society: Washington, DC, USA, 2003; pp. 123–132. [[CrossRef](#)]
70. Boschloo, G.; Lindström, H.; Magnusson, E.; Holmberg, A.; Hagfeldt, A. Optimization of dye-sensitized solar cells prepared by compression method. *J. Photochem. Photobiol. A Chem.* **2002**, *148*, 11–15. [[CrossRef](#)]
71. Li, X.; Lin, H.; Li, J.; Li, X.; Cui, B.; Zhang, L. A numerical simulation and impedance study of the electron transport and recombination in binder-free TiO<sub>2</sub> film for flexible dye-sensitized solar cells. *J. Phys. Chem. C* **2008**, *112*, 13744–13753. [[CrossRef](#)]
72. Zhao, X.; Lin, H.; Li, X.; Li, J. The effect of compression on electron transport and recombination in plastic TiO<sub>2</sub> photoanodes. *Electrochim. Acta* **2011**, *56*, 6401–6405. [[CrossRef](#)]
73. Yang, H.; Liu, W.; Xu, C.; Fan, D.; Cao, Y.; Xue, W. Laser sintering of TiO<sub>2</sub> films for flexible dye-sensitized solar cells. *Appl. Sci.* **2019**, *9*, 823. [[CrossRef](#)]

74. Huang, W.M.; Tsai, J.K.; Wu, T.C.; Meen, T.H. Improvement of Dye-sensitized Solar Cells by Using Compact and Pressed Layer of TiO<sub>2</sub>. In Proceedings of the 2022 5th IEEE International Conference on Knowledge Innovation and Invention, Hualien, Taiwan, 22–24 July 2022; pp. 63–68. [CrossRef]
75. Yoshida, T.; Oekermann, T.; Okabe, K.; Schlettwein, D.; Funabiki, K.; Minoura, H. Cathodic Electrodeposition of ZnO/EosinY Hybrid Thin Films from Dye Added Zinc Nitrate Bath and Their Photoelectrochemical Characterizations. *Electrochemistry* **2002**, *70*, 470–487. [CrossRef]
76. Tan, W.; Chen, J.; Zhou, X.; Zhang, J.; Lin, Y.; Li, X.; Xiao, X. Preparation of nanocrystalline TiO<sub>2</sub> thin film at low temperature and its application in dye-sensitized solar cell. *J. Solid State Electrochem.* **2009**, *13*, 651–656. [CrossRef]
77. Miyasaka, T.; Kijitori, Y. Low-Temperature Fabrication of Dye-Sensitized Plastic Electrodes by Electrophoretic Preparation of Mesoporous TiO<sub>2</sub> Layers. *J. Electrochem. Soc.* **2004**, *151*, A1767. [CrossRef]
78. Ferrere, S.; Gregg, B.A. Large increases in photocurrents and solar conversion efficiencies by UV illumination of dye sensitized solar cells. *J. Phys. Chem. B.* **2001**, *105*, 7602–7605. [CrossRef]
79. Rawolle, M.; Niedermeier, M.A.; Kaune, G.; Perlich, J.; Lellig, P.; Memesa, M.; Cheng, Y.-J.; Gutmann, J.S.; Müller-Buschbaum, P. Fabrication and characterization of nanostructured titania films with integrated function from inorganic–organic hybrid materials. *Chem. Soc. Rev.* **2012**, *41*, 5131–5142. [CrossRef]
80. Orilall, M.C.; Wiesner, U. Block copolymer based composition and morphology control in nanostructured hybrid materials for energy conversion and storage: Solar cells, batteries, and fuel cells. *Chem. Soc. Rev.* **2011**, *40*, 520–535. [CrossRef]
81. Nilsson, E.; Sakamoto, Y.; Palmqvist, A.E.C. Low-temperature synthesis and HRTEM analysis of ordered mesoporous anatase with tunable crystallite size and pore shape. *Chem. Mater.* **2011**, *23*, 2781–2785. [CrossRef]
82. Shibata, H.; Ogura, T.; Mukai, T.; Ohkubo, T.; Sakai, H. Direct synthesis of mesoporous titania particles having a crystalline wall. *J. Am. Chem. Soc.* **2005**, *127*, 16396–16397. [CrossRef] [PubMed]
83. Longo, C.; Nogueira, A.F.; De Paoli, M.A.; Cachet, H. Solid-state and flexible dye-sensitized TiO<sub>2</sub> solar cells: A study by electrochemical impedance spectroscopy. *J. Phys. Chem. B* **2002**, *106*, 5925–5930. [CrossRef]
84. Longo, C.; Freitas, J.; De Paoli, M.A. Performance and stability of TiO<sub>2</sub>/dye solar cells assembled with flexible electrodes and a polymer electrolyte. *J. Photochem. Photobiol. A Chem.* **2003**, *159*, 33–39. [CrossRef]
85. Haseloh, S.; Choi, S.Y.; Mamak, M.; Coombs, N.; Petrov, S.; Choprab, N.; Ozin, G.A. Towards flexible inorganic ‘mesomaterials’: One-pot low temperature synthesis of mesostructured nanocrystalline titania. *Chem. Commun.* **2004**, *4*, 1460–1461. [CrossRef] [PubMed]
86. Gutiérrez-Tauste, D.; Zumeta, I.; Vigil, E.; Hernández-Fenollosa, M.A.; Domènech, X.; Ayllón, J.A. New low-temperature preparation method of the TiO<sub>2</sub> porous photoelectrode for dye-sensitized solar cells using UV irradiation. *J. Photochem. Photobiol. A Chem.* **2005**, *175*, 165–171. [CrossRef]
87. Nemoto, J.; Sakata, M.; Hoshi, T.; Ueno, H.; Kaneko, M. All-plastic dye-sensitized solar cell using a polysaccharide film containing excess redox electrolyte solution. *J. Electroanal. Chem.* **2007**, *599*, 23–30. [CrossRef]
88. Tebby, Z.; Babot, O.; Toupance, T.; Park, D.H.; Campet, G.; Delville, M.H. Low-temperature UV-processing of nano-crystalline nanoporous Thin TiO<sub>2</sub> films: An original route toward plastic electrochromic systems. *Chem. Mater.* **2008**, *20*, 7260–7267. [CrossRef]
89. Tebby, Z.; Babot, O.; Michau, D.; Hirsch, L.; Carlos, L.; Toupance, T. A simple route towards low-temperature processing of nanoporous thin films using UV-irradiation: Application for dye solar cells. *J. Photochem. Photobiol. A Chem.* **2009**, *205*, 70–76. [CrossRef]
90. Miyasaka, T.; Kijitori, Y.; Murakami, T.N.; Kimura, M.; Uegusa, S. Efficient Nonsintering Type Dye-sensitized Photocells Based on Electrophoretically Deposited TiO<sub>2</sub> Layers. *Chem. Lett.* **2002**, *31*, 1250–1251. [CrossRef]
91. Murakami, T.N.; Kijitori, Y.; Kawashima, N.; Miyasaka, T. UV Light-assisted Chemical Vapor Deposition of TiO<sub>2</sub> for Efficiency Development at Dye-sensitized Mesoporous Layers on Plastic Film Electrodes. *Chem Lett.* **2003**, *32*, 1076–1077. [CrossRef]
92. Murakami, T.N.; Kijitori, Y.; Kawashima, N.; Miyasaka, T. Low temperature preparation of mesoporous TiO<sub>2</sub> films for efficient dye-sensitized photoelectrode by chemical vapor deposition combined with UV light irradiation. *J. Photochem. Photobiol. A Chem.* **2004**, *164*, 187–191. [CrossRef]
93. Uchida, S.; Tomiha, M.; Takizawa, H.; Kawaraya, M. Flexible dye-sensitized solar cells by 28 GHz microwave irradiation. *J. Photochem. Photobiol. A Chem.* **2004**, *164*, 93–96. [CrossRef]
94. Kado, T.; Yamaguchi, M.; Yamada, Y.; Hayase, S. Low Temperature Preparation of Nano-porous TiO<sub>2</sub> Layers for Plastic Dye Sensitized Solar Cells. *Chem. Lett.* **2003**, *32*, 1056–1057. [CrossRef]
95. ISO 15184:2020; Paints and varnishes–Determination of films hardness by pencil test. International Organization for Standardization: Geneva, Switzerland, 2012. Available online: <https://www.iso.org/standard/76044.html> (accessed on 26 June 2023).
96. Yamaguchi, T.; Tobe, N.; Matsumoto, D.; Arakawa, H. Highly efficient plastic substrate dye-sensitized solar cells using a compression method for preparation of TiO<sub>2</sub> photoelectrodes. *Chem. Commun.* **2007**, *45*, 4767–4769. [CrossRef]
97. Yamaguchi, T.; Tobe, N.; Matsumoto, D.; Nagai, T.; Arakawa, H. Highly efficient plastic-substrate dye-sensitized solar cells with validated conversion efficiency of 7.6%. *Sol. Energy Mater. Sol. Cells* **2010**, *94*, 812–816. [CrossRef]
98. Grinis, L.; Dor, S.; Ofir, A.; Zaban, A. Electrophoretic deposition and compression of titania nanoparticle films for dye-sensitized solar cells. *J. Photochem. Photobiol. A Chem.* **2008**, *198*, 52–59. [CrossRef]

99. Miyoshi, K.; Numao, M.; Ikegami, M.; Miyasaka, T. Effect of Thin TiO<sub>2</sub> Buffer on the Performance of Plastic-based Dye-sensitized Solar Cells Using Indoline Dye. *Electrochemistry* **2007**, *76*, 158–160. [[CrossRef](#)]
100. Lee, K.-M.; Wu, S.-J.; Chen, C.-Y.; Wu, C.-G.; Ikegami, M.; Miyoshi, K.; Miyasaka, T.; Ho, K.-C. Efficient and stable plastic dye-sensitized solar cells based on a high light-harvesting ruthenium sensitizer. *J. Mater. Chem.* **2009**, *19*, 5009–5015. [[CrossRef](#)]
101. Haque, S.A.; Palomares, E.; Upadhyaya, H.M.; Otley, L.; Potter, R.J.; Holmes, A.B.; Durrant, J.R. Flexible dye sensitized nanocrystalline semiconductor solar cells. *Chem. Commun.* **2003**, *3*, 3008–3009. [[CrossRef](#)]
102. Lee, K.-M.; Hsu, Y.-C.; Ikegami, M.; Miyasaka, T.; Thomas, K.R.J.; Lin, J.T.; Ho, K.-C. Co-sensitization promoted light harvesting for plastic dye-sensitized solar cells. *J. Power Sources* **2011**, *196*, 2416–2421. [[CrossRef](#)]
103. Kim, J.; Lee, H.; Kim, D.Y.; Seo, Y. Resonant multiple light scattering for enhanced photon harvesting in dye-sensitized solar cells. *Adv. Mater.* **2014**, *26*, 5192–5197. [[CrossRef](#)]
104. Kim, J.; Lee, H.; Kim, D.Y.; Kim, S.; Seo, Y. Cobalt-based electrolytes for efficient flexible dye-sensitized solar cells. *MRS Adv.* **2019**, *4*, 481–489. [[CrossRef](#)]
105. Pichot, F.; Pitts, J.R.; Gregg, B.A. Low-temperature sintering of TiO<sub>2</sub> colloids: Application to flexible dye-sensitized solar cells. *Langmuir* **2000**, *16*, 5626–5630. [[CrossRef](#)]
106. Zhang, D.; Yoshida, T.; Minoura, H. Low-temperature fabrication of efficient porous titania photoelectrodes by hydrothermal crystallization at the solid/gas interface. *Adv. Mater.* **2003**, *15*, 814–817. [[CrossRef](#)]
107. Senthilkumar, S.; Rajendran, A. Biosynthesis of TiO<sub>2</sub> nanoparticles using *Justicia gendarussa* leaves for photocatalytic and toxicity studies. *Res. Chem. Intermed.* **2018**, *44*, 5923–5940. [[CrossRef](#)]
108. Jin Joo, J.; Kwon, S.G.; Yu, T.; Cho, M.; Lee, J.; Yoon, J.; Hyeon, T. Large-scale synthesis of TiO<sub>2</sub> nanorods via nonhydrolytic sol-gel ester elimination reaction and their application to photocatalytic inactivation of *E. coli*. *J. Phys. Chem. B* **2005**, *109*, 15297–15302. [[CrossRef](#)]
109. Filippo, E.; Carlucci, C.; Capodilupo, A.L.; Perulli, P.; Conciauro, F.; Corrente, G.A.; Gigli, G.; Ciccarella, G. Enhanced photocatalytic activity of pure anatase TiO<sub>2</sub> and Pt-TiO<sub>2</sub> nanoparticles synthesized by green microwave-assisted route. *Mater. Res.* **2015**, *18*, 473–481. [[CrossRef](#)]
110. Tao, P.; Li, Y.; Rungta, A.; Viswanath, A.; Gao, J.; Benicewicz, B.C.; Siegel, R.W.; Schadler, L.S. TiO<sub>2</sub> nanocomposites with high refractive index and transparency. *J. Mater. Chem.* **2011**, *21*, 18623–18629. [[CrossRef](#)]
111. Saleh, T.A. Structural characterization of hybrid materials. In *Polymer Hybrid Materials and Nanocomposites*, 1st ed.; Payne, E., Mearns, J., Eds.; Elsevier: Amsterdam, The Netherlands, 2021; pp. 213–240. [[CrossRef](#)]
112. Wante, H.P.; Aidan, J.; Ezike, S.C. Efficient dye-sensitized solar cells (DSSCs) through atmospheric pressure plasma treatment of photoanode surface. *Curr. Res. Green Sustain. Chem.* **2021**, *4*, 100218. [[CrossRef](#)]
113. Feldt, S.M.; Lohse, P.W.; Kessler, F.; Nazeeruddin, M.K.; Grätzel, M.; Boschloo, G.; Hagfeldt, A. Regeneration and recombination kinetics in cobalt polypyridine based dye-sensitized solar cells, explained using Marcus theory. *Phys. Chem. Chem. Phys.* **2013**, *15*, 7087–7097. [[CrossRef](#)] [[PubMed](#)]
114. Masud, N.; Kim, H.K. Redox Shuttle-Based Electrolytes for Dye-Sensitized Solar Cells: Comprehensive Guidance, Recent Progress, and Future Perspective. *ACS Omega* **2023**, *8*, 6139–6163. [[CrossRef](#)] [[PubMed](#)]
115. Fabregat-Santiago, F.; Bisquert, J.; Palomares, E.; Otero, L.; Kuang, D.; Zakeeruddin, S.M.; Graetzel, M. Correlation between Photovoltaic Performance and Impedance Spectroscopy of Dye-Sensitized Solar Cells Based on Ionic Liquids. *J. Phys. Chem. C* **2007**, *111*, 6550–6560. [[CrossRef](#)]
116. Guillén, E.; Fernández-Lorenzo, C.; Alcántara, R.; Martín-Calleja, J.; Anta, J.A. Solvent-free ZnO dye-sensitized solar cells. *Sol. Energy Mater. Sol. Cells* **2009**, *93*, 1846–1852. [[CrossRef](#)]
117. Juang, S.S.-Y.; Lin, P.-Y.; Lin, Y.-C.; Chen, Y.-S.; Shen, P.-S.; Guo, Y.-L.; Wu, Y.-C.; Chen, P. Energy harvesting under dim-light condition with dye-sensitized and perovskite solar cells. *Front. Chem.* **2019**, *7*, 209. [[CrossRef](#)]
118. Idígoras, J.; Pellejà, L.; Palomares, E.; Anta, J.A. The redox pair chemical environment influence on the recombination loss in dye-sensitized solar cells. *J. Phys. Chem. C* **2014**, *118*, 3878–3889. [[CrossRef](#)]
119. Holliman, P.J.; Mohsen, M.; Connell, A.; Kershaw, C.P.; Meza-Rojas, D.; Jones, E.W.; Geatches, D.; Sen, K.; Hsiao, Y.-W. Double linker triphenylamine dyes for dye-sensitized solar cells. *Energies* **2020**, *13*, 4637. [[CrossRef](#)]
120. Sharma, K.; Sharma, V.; Sharma, S.S. Dye-Sensitized Solar Cells: Fundamentals and Current Status. *Nanoscale Res. Lett.* **2018**, *13*, 381. [[CrossRef](#)]
121. Boschloo, G.; Hagfeldt, A. Characteristics of the iodide/triiodide redox mediator in dye-sensitized solar cells. *Acc. Chem. Res.* **2009**, *42*, 1819–1826. [[CrossRef](#)]
122. Kalaigan, G.P.; Kang, Y.S. A review on mass transport in dye-sensitized nanocrystalline solar cells. *J. Photochem. Photobiol. C* **2006**, *7*, 17–22. [[CrossRef](#)]
123. Biswas, S.; Kim, H. Solar cells for indoor applications: Progress and development. *Polymers* **2020**, *12*, 1338. [[CrossRef](#)] [[PubMed](#)]
124. De Rossi, F.; Pontecorvo, T.; Brown, T.M. Characterization of photovoltaic devices for indoor light harvesting and customization of flexible dye solar cells to deliver superior efficiency under artificial lighting. *Appl. Energy* **2015**, *156*, 413–422. [[CrossRef](#)]

**Disclaimer/Publisher’s Note:** The statements, opinions and data contained in all publications are solely those of the individual author(s) and contributor(s) and not of MDPI and/or the editor(s). MDPI and/or the editor(s) disclaim responsibility for any injury to people or property resulting from any ideas, methods, instructions or products referred to in the content.